

**CONTROLLED SYNTHESIS OF NANOSTRUCTURES
AND THEIR OPTICAL PROPERTIES**

KHOH RONG LUN

(B.Sc.(Hons.), NUS)

**A THESIS SUBMITTED
FOR THE DEGREE OF MASTER OF SCIENCE**

DEPARTMENT OF CHEMISTRY

NATIONAL UNIVERSITY OF SINGAPORE

2011

Acknowledgement

I would like to express my gratitude to the many people who have made this thesis possible.

The first person I would like to thank would be my supervisor, Associate Professor Chin Wee Shong. It had been a fruitful period spent with her from my Honours year to the end of my M.Sc. course. She had been an exemplary mentor who was patient, genuine and generous with her support. I am grateful for the many opportunities she had provided me, from having the chance to mentor junior Honours students to participating in conferences both in Singapore and Malaysia. Also, she was always encouraging of new ideas and that made my days spent in lab particularly rewarding. I would look forward to having discussions with her for she would always provide good suggestions and impress me with her professionalism.

I would like to thank Professor Andrew Wee and Associate Professor Thorsten Wohland for being my referees, without whom I would not be able to defer my MOE bond fulfilment and embark on my graduate studies.

My fellow group members included: Dr. Xu Hairuo, Dr. Neo Min Shern, Dr. Li Guoshuo, Madam Liang Eping, Ms. Teo Tingting Sharon, Ms. Loh Pui Yee, Ms. Tan Zhi Yi and Mr. Huang Baoshi Barry. It was with their immense support and active contribution in ideas that helped made the course enjoyable. In particular, I would like to thank Dr. Xu Hairuo, who was also mentor for my Honours project, for leaving me with such good experience with research that I was encouraged to pursue a

research-based higher degree. In addition, I would like to thank the support and laboratory staff from Department of Chemistry, Department of Biological Sciences and Department of Material Engineering for being big-hearted and helpful. It was with their help that facilitated the resolving of administrative issues and characterization of samples.

Furthermore, I would like to thank my peers for being such pillars of support. They included friends from NUS Students' Science Club, Ms. Chen Shuhui, Mr. Chan Xin Wei, Mr. Andy Chia, Mr. Lee Wei Kit, Mr. Wang Wei Yang, Mr. Nai Chang Tai and Ms. Chan Zi Ping. In particular, it had been an awesome experience mentoring Ms. Chen Shuhui and Mr. Chan Xin Wei.

Finally, I would like to thank my parents Mr. Khoh Kian Hock and Mdm Chiang Swee Lan for being forever tolerant and supportive of my decisions and actions.

Table of Contents

Summary	vii
List of Publications	ix
List of Figures	x
List of Tables	xii
Chapter 1 Introduction	1
1.1 Background	1
1.2 Size-dependent Properties: The Effect and Control of Sizes	2
1.2.1 Semiconductor Nanocrystals	2
1.2.2 Metal Nanocrystals	4
1.3 Shape-dependent Properties: The Effect and Control of Shapes ...	5
1.4 Multi-component Nanocrystals	7
1.4.1 Doped Nanocrystals	8
1.4.2 Heterostructured Nanocrystals	9
1.4.3 Hybrid Nanocrystals	12
1.5 Synthetic Methodologies of Nanocrystals	13
1.5.1 Solution Synthesis of Nanocrystals	15
1.5.2 Synthesis of Doped Nanocrystals	16
1.5.3 Synthesis of Heterostructured and Hybrid Nanocrystals ...	17
1.6 Objective and Scope of the Thesis	18

1.7	References	19
Chapter 2	Experimental	24
2.1	Chemical reagents	24
2.2	Preparation procedures	25
2.2.1	Preparation of CdS CdSe CdS nanorods	25
2.2.2	Preparation of CdSe CdS CdSe nanorods	26
2.2.3	Preparation of gold-deposited CdS CdSe CdS and CdSe CdS CdSe nanorods	26
2.2.4	Preparation of cadmium thiobenzoate and zinc thiobenzoate precursors	27
2.2.5	Preparation of CdS quantum dots	28
2.2.6	Preparation of CdS-seeded Mn ²⁺ -doped ZnS	28
2.2.7	Preparation of gold-decorated CdS-seeded Mn ²⁺ -doped ZnS	29
2.3	Characterization Techniques	29
2.3.1	Transmission Electron Microscopy and High Resolution Transmission Electron Microscopy	29
2.3.2	Ultraviolet-visible Absorption Spectroscopy	30
2.3.3	Steady-state Photoluminescence Spectroscopy	30
2.3.4	Elemental Analysis	31
2.3.5	Thermal Gravimetric Analysis	31
2.3.6	Powder X-Ray Diffraction	32

2.4	References	32
Chapter 3	Gold Deposition on CdSe CdS Heterostructured Sandwiched Nanorods	33
3.1	Synthesis and characterization of the CdS CdSe CdS and CdSe CdS CdSe sandwiched nanorods	34
3.2	Optical properties of the CdS CdSe CdS and CdSe CdS CdSe sandwiched nanorods	38
3.3	Deposition of Au on the CdS CdSe CdS and CdSe CdS CdSe sandwiched nanorods	41
3.4	Optical properties of the Au-deposited CdS CdSe CdS and CdSe CdS CdSe sandwiched nanorods	46
3.5	Summary	49
3.6	References	49
Chapter 4	Gold Deposition on CdS/ZnS:Mn²⁺ Doped-and-Seeded Heterostructured Nanocrystals	51
4.1	Synthesis and characterization of the CdS seeds	52
4.2	Synthesis and characterization of the CdS/ZnS seeded nanorods	55
4.3	Synthesis and characterization of the CdS/ZnS:Mn ²⁺ doped-and-seeded nanorods	59
4.4	Gold deposition on the CdS/ZnS:Mn ²⁺ hybrid nanorods	62

4.5	Summary	64
4.6	References	65
Chapter 5	Conclusions and Outlook	67

Summary

The ability to synthesize nanocrystals with good control over their sizes and shapes had been a milestone for nanoscience. Works in the early days of nanoscience were focused on understanding the underlying factors that affect sizes and shapes. That had been done with much success, judging from the overwhelming number of literatures that dealt with such discussions. A few parameters were subsequently identified: monomer concentration, reaction temperature, choice of capping agents and method of synthesis. The manipulation of these parameters then became a cornerstone in achieving nanocrystals of a myriad of morphologies. Despite the apparent success the control over engineering of nanocrystals, there has been much lesser understanding towards the underlying principles behind the outcomes of some syntheses. This issue became more acute as research progressed to investigate multi-component nanocrystals where different materials of various shapes and sizes were combined.

The focus of the works in this thesis was on the issues of synthesis and optical properties of multi-component nanocrystals comprising metal sulfide/selenide nanorods. In Chapter 3, we had successfully synthesized the sandwich CdS|CdSe|CdS and CdSe|CdS|CdSe nanorods and followed by the deposition of gold nanoparticles onto system. Besides obtaining insights to the deposition behaviours of the gold nanoparticles, we also observed interesting optical properties of the overall nanoparticle system. We observed the gold deposition first occurred randomly along

the sides of the nanorods due to defect growths, but the gold nanoparticles eventually grew larger at the tips of nanorods because of Ostwald ripening.

In Chapter 4, we tapped on prior know-how of our research group to synthesize a series of multi-component nanocrystals using rational stepwise synthesis processes. We followed the optical properties of the nanoparticles systematically while components were added one-by-one. In particular, we presented a case study which involved the simultaneous presence of two potential quenchers, i.e. gold nanoparticles and Mn^{2+} dopants. We observed that gold nanoparticles were better quenchers than the Mn^{2+} dopants, in affecting the band gap emission of the seeded semiconductor nanocrystals.

List of Publications

Syntheses and Optical Properties of Multi-Component Hybrid Heterostructured Nanoparticles

R. L. Khoh, S. Chen, W. S. Chin *manuscript in preparation.*

Preferred Gold Deposition Sites on Heterostructured Sandwiched Nanorods and the Consequential Changes in Optical Properties

R. L. Khoh, X. W. Chan, W. S. Chin *manuscript in preparation.*

List of Figures

- 1.1 A plot for illustrating nucleation and growth during the preparation of nanoparticles. 14
- 3.1 Cartoon illustrations of (a) ABA and (b) BAB nanorods, where A denotes CdS and B denotes CdSe. 35
- 3.2 TEM images of CdS|CdSe|CdS and CdSe|CdS|CdSe nanorods. 35
- 3.3 XRD patterns of CdS|CdSe|CdS and CdSe|CdS|CdSe nanorods and schematic illustration of the wurtzite crystal structure. 36
- 3.4 Chemical structures of (a) trioctylphosphine oxide and (b) 1-tetradecylphosphonic acid. 37
- 3.5 HRTEM images of CdS|CdSe|CdS and CdSe|CdS|CdSe nanorods. 38
- 3.6 UV-Vis spectra of (a) pure CdSe, (b) pure CdS and (c) a 1:1 physical mixture of CdS and CdSe nanorods. 39
- 3.7 PL spectra of (a) CdS, (b) CdSe and (c) a 1:1 physical mixture of CdS and CdSe nanorods. 39
- 3.8 (a) & (c) UV-Vis and (b) & (d) PL ($\lambda_{\text{excitation}} = 525 \text{ nm}$) spectra of the CdS|CdSe|CdS (top, purple) and CdSe|CdS|CdSe (bottom, red) sandwiched nanorods respectively. 40
- 3.9 Possible morphologies for Au deposition on the CdS|CdSe|CdS structure: (a) Au deposited randomly along the nanorod, (b) Au selectively deposited on the tips of the nanorod and (c) Au selectively deposited on the lower band gap (CdSe) segment of the nanorod. 42
- 3.10 TEM images of Au deposition on the ABA nanorods at (a) 10 min, (b) 30 min and (c) 60 min after injection of Au precursor. 43
- 3.11 Distribution histograms relating the number of Au nanoparticles deposited on the various positions along the CdS|CdSe|CdS nanorod at (a) 10 min, (b) 30 min and (c) 60 min after injection of Au precursor. 44
- 3.12 TEM image of Au deposition on the CdSe|CdS|CdSe nanorods 60 min after injection of Au precursor. 45

-
- 3.13 (a) & (c) UV-Vis and (b) & (d) PL spectra of Au-deposited CdS|CdSe|CdS (top) and CdSe|CdS|CdSe (bottom) nanorods at 10 min (red), 30 min (green), 45 min (blue) and 60 min (pink) after injection of the gold-precursor. 47
- 3.14 Temporal evolution of (a) & (c) UV-Vis and (b) & (d) PL spectra of Au deposition on the CdS|CdSe|CdS (top) and CdSe|CdS|CdSe (bottom) nanorods monitored at three- and six-minute intervals respectively. 48
- 4.1 TGA curve for the decomposition of CdTB precursor from room temperature to 600 °C. 53
- 4.2 (a) UV-Vis absorption (red line) and PL (black line) spectrum of the CdS seeds prepared. (b) XRD pattern of the CdS seeds fitted to the zinc blende standard JCPDS 10-0454. 54
- 4.3 (a) Representative HRTEM image of the seeded CdS/ZnS nanorods prepared. (b) UV-Vis absorption (red line) and PL (black line) spectrum of the CdS-seeded ZnS nanorods. (c) Cartoon illustrating the change in wave function as the ZnS nanorod was overgrown on the CdS seeds. (d) XRD patterns of the CdS/ZnS nanorods prepared fitted to JCPDS: 05-0566. (e) Representative TEM image of the CdS/ZnS prepared. 57
- 4.4 (a) Representative TEM image of the CdS-seeded Mn²⁺-doped ZnS nanorods, CdS/ZnS:Mn²⁺. (b) UV-Vis absorption (red line) and PL emission (black line) spectrum of the CdS/ZnS:Mn²⁺ nanorods, CdS/ZnS:Mn²⁺. 60
- 4.5 Schematics showing energy transfer from ZnS host and CdS to Mn²⁺ dopants. 62
- 4.6 (a) Representative TEM image of Au decorated nanorods, Au-CdS/ZnS:Mn²⁺. (b) PL spectrum of CdS/ZnS:Mn²⁺ (black) and Au-CdS/ZnS:Mn²⁺ (red). 64

List of Tables

1.1	Different morphologies of heterostructured nanocrystals.	10
1.2	Different types of semiconductor-semiconductor nanocrystals illustrated using concentric core/shell nanocrystals.	11
2.1	Chemicals and solvents used and their respective percentage purities and sources.	24
3.1	Average diameter of Au nanoparticles on both the side facets and tips of the CdS CdSe CdS nanorod at 10 min, 30 min and 60 min intervals after injection of Au precursor.	43

Chapter 1

Introduction

1.1 Background

Nanomaterials have attracted the interests of scientists and engineers alike for nearly three decades and there is no sign for the level of interest to be abating. What then has fuelled this immense interest? Firstly, nanomaterials display different properties compared to their bulk counterparts. Besides the excitement to account for the differences from the viewpoint of fundamental science, having different properties also suggests that we can expand the range of applications of these materials from what we already knew of the bulk materials. This could be exemplified by the light-emitting diodes made of CdSe nanocrystals.¹ Whereas the bulk CdSe was known to be monochromic, CdSe nanocrystals could be made to emit in the range of red to yellow. Secondly, the nanometer size of particles allowed them to be useful in areas such as in biological systems^{2,3} where the bigger particles were not.

As such, there had been a strong research buzz over the different aspects of nanomaterials, most notably in areas involving the control and manipulation over their growth, sizes, and shapes – all of which would determine their properties, applications and performances. At the infancy stage of nanomaterials research, majority of work dealt with single-material nanocrystals. Two most commonly studied types of nanomaterial included the semiconductors (e.g. InP^{4,5} and GaN⁶) and metals (e.g. Au^{7,8} and Ag^{9,10}).

Although there had been significant breakthroughs in realising various controls and applications for the single-material nanocrystals, the study on nanocrystals is far from being a sunset research subject. The feats for single-material nanomaterials laid a solid ground for synthesizing nanocrystals of a combination of materials and of even more varied morphologies. These multi-component nanocrystals are highly attractive candidates for scientific studies and applications because they are often associated with greater robustness and/or novel properties. However, the multi-component nanocrystals are often not well-understood at the fundamental level and this in turn stifles attempts in gaining good control attained with the single-material nanocrystals.

1.2 Size-dependent Properties: The Effect and Control of Sizes

As mentioned earlier, nanocrystals have properties different from their bulk counterparts. The reason behind such behaviours, however, goes further than just the size alone. In fact, the reason varies with the material of discussion. In this section, the peculiarity of the semiconductor and metallic nanocrystals materials would be explained and elaborated.

1.2.1 Semiconductor Nanocrystals

When the size of a semiconductor particle decreases to approximately its characteristic Bohr radius, the electronic structure of the particle would change from continuous bands to discrete electronic levels. Exciton pairs generated from such particle would be confined and the particle is commonly known to be experiencing “quantum confinement”. This phenomenon typically occurs when the dimension of

the semiconductor particle is in the nanometer range and it has drastic impacts on the electronic and optical properties of these nanocrystals.

As the size of the nanoparticle continues to decrease, the energy gap between the valence and conduction bands would broaden. This can be understood by comparing the nanoparticle against the particle-in-a-box model. CdSe had been used to demonstrate this in several reports,^{11,12} where its absorption peaks were blue-shifted with a decreasing nanoparticle size. Furthermore, Mittleman *et al.*¹³ had shown that CdSe had fewer absorption features as the size decreases due to a concentration of oscillator strengths to lesser electronic transitions. More recently, Bowers II *et al.*¹⁴ reported white light emission from magic-sized CdSe¹⁵ nanocrystals which were ~ 1.5 nm in size. This was yet another consequence of size whereby the small size of CdSe resulted in the interaction of exciton pairs at the nanocrystals surface causing a broad emission over the entire visible range.¹⁴

The sheer size of nanocrystals also considerably lowers their melting points. These particles have significant surface area-to-volume ratio with high surface energy as well as an abundance of the uncoordinated surface atoms. Hence there is a great driving force towards melting in a bid to lower the surface energy. For instance, the melting point of nanosized CdS was known to be approximately 1000 K lower than that of bulk CdS.¹⁶

Given that size plays a big role in affecting properties of semiconductor nanocrystals, the control of sizes is understandably important. In most cases, the use of capping agents is the method of choice to control sizes in solution synthesis. The principles of this method lie in providing steric hindrance and energetics considerations. Capping agents used are usually organic molecules with lone pairs of

electrons (via atoms like N, O and S) available for coordination with the surface cations. Presence of these organic molecules would prevent further growth of the nanocrystals. It is also entropically unfavourable for the capped nanocrystals to aggregate as that would cause the capping agents to be more densely packed than if the nanocrystals were spaced apart.

1.2.2 Metal Nanocrystals

Unlike semiconductors that undergo quantum confinement at the nanoscale, metal nanocrystals' differ in properties from their bulk due to the coherent interaction between the metal electrons and incoming electromagnetic fields. A surface charge separation would result. There would be strong absorption of electromagnetic waves of frequency that matches the resonance frequency of the electrons motion. This absorption is termed 'surface plasmon resonance' (SPR).

Interestingly, how the size affects the optical properties of metal nanocrystals depend firstly on the size range of the particles. Based on Mie's theory developed in 1908, larger metal nanocrystals (beyond ~ 20 nm) have red-shifted and broadened absorption SPR peak.¹⁷ The broadening effect was attributed to the non-homogeneous polarization of surface electrons for larger nanocrystals.¹⁷ For smaller metal nanocrystals (smaller than ~ 20 nm), the absorption was predicted to be independent of the size. However, for even smaller metal nanocrystals (~2 – 3 nm or less), Hostetler *et al.*¹⁸ observed that SPR absorption was totally washed out. This was explained as the onset of quantization below a critical size which resulted in the loss of the SPR absorption.¹⁸

Bulk sized metals have long been used in the catalysis of a myriad of reactions. Metal nanocrystals are expected to possess catalytic properties as well. In fact, the high surface area-to-volume ratio of the metal nanocrystals is advantageous in the way that more catalytic sites are exposed. Narayanan and El-Sayed illustrated this point when they showed how Pt nanocrystals with greater fraction of surface atoms resulted in increased catalytic activities.¹⁹

As with semiconductor nanocrystals, the main approach to control the size of metal nanocrystals in solution synthesis is through employing capping agents and manipulating the reaction rates.

1.3 Shape-dependent Properties: The Effect and Control of Shapes

Other than sizes, shapes of nanocrystals also affect their properties. This is partly due to the different surface facets and the presence of more edges and corners in the nanocrystals. Mostafa *et al.*²⁰ had recently shown experimentally how the Pt nanocrystals of similar sizes but of dissimilar shapes exhibit different catalytic properties. CdSe nanorods also have the ability to emit linearly polarized light unlike CdSe quantum dots.²¹

There are four main factors in the determination of the shapes of nanocrystals in solution syntheses, namely: monomer concentration, reaction temperature, choice of capping agents and method of synthesis.

Peng and Peng¹⁵ had use CdSe as a case study to explain how monomer concentration affected shapes of nanocrystals. Generally, elongated nanocrystals such as nanorods and nanotetrapods have higher chemical potential than their spherical counterparts, as expected from the higher surface area. To favour an elongated

morphology, a high monomer concentration is desirable. They argued that nanoparticle growth follows a diffusion-controlled process rather than a reaction-controlled growth which fails to explain the ripening of nanocrystals at low monomer concentrations. At a high monomer concentration, monomers would diffuse into the diffusion sphere of the nanocrystals. However, as the nanocrystals elongate into nanorods, the tips facets have higher chemical potential and would thus receive more monomers and the nanorods would continue to elongate.

Temperature plays a critical role in the determination of the crystal phase of the nanocrystals which subsequently affects the final evolved nanoparticle shape under a prolonged reaction. As the reaction temperature increases, the more predominant crystal phase of the nanocrystals changes from one that is thermodynamically stable to one that is kinetically stable. At a low reaction temperature, CdS exists in zinc blende phase^{22,23} which leads to the formation of multipods.

Another parameter to manipulate nanoparticle shapes is the choice of capping agent. A mixture of capping agents can be used to achieve a gradient in the binding strength of the capping agents with the different facets of nanocrystals. The facets where capping agents are less strongly bound would grow faster than others. An example of a mixture of capping agents is cetyltrimethylammonium bromide and tetraoctylammonium bromide which are both used in the synthesis of Au nanorods.²⁴

Besides acting as capping agents, organic molecules in the form of dendrimers can aid in shaping noble metal nanocrystals. Vassilieff *et al.*²⁵ showed how an increasing generation number of dendrimers, thus an increasing openness of the structure, can lead to an evolution of shape from sphere to cube for Ag nanocrystals.

Lastly, pre-formed nuclei of a desired crystal phase or shape can be added such that heterogeneous nucleation occurs. Heterogeneous nucleation works on the basis that growth on the pre-formed nuclei is more energetically feasible than separated nucleation. Jana *et al.* had previously used this method to form long wires of Ag from small spherical Ag.²⁶

1.4 Multi-Component Nanocrystals

Multi-component nanocrystals are typically made up of at least two types of nanomaterials. The burgeoning interest in the research on multi-component nanocrystals is a natural progression in research direction made possible by the success attained in the growth control of single-material nanocrystals. A growing demand for nanocrystals that possess multi-functionalities is a major driving force for the surge in this research trend. For example, bifunctional Au-Fe₃O₄ nanocrystals had been synthesized, with Au useful in assembly works and magnetic Fe₃O₄ practical in sensory works.²⁷ Another interesting aspect of such multi-component nanocrystals is that they may display novel properties which are not present in the individual components.

An introduction to the various types of multi-component nanocrystals covered in this thesis would be provided in the following subsections.

1.4.1 Doped Nanocrystals

Doped nanocrystals are obtained when impurities (dopants) are introduced. Even though the amount of impurities present may be as low as $< 1\%$,²⁸ they are able to bring about major changes to the properties displayed by the nanocrystals. Dopants that are present in the interstitial or substitutional positions²⁹ are known to result in novel optical and/or magnetic properties whereas dopants that are only residing on the nanocrystals surfaces³⁰ do not bring about new properties.

Doping nanocrystals with transition metal (Mn^{2+} , Cu^{2+})^{31,32} or rare-earth metal ions (Eu^{3+} , Tb^{3+})³³ provides a mean to modify the optical properties of the original nanocrystals by making new relaxation pathways available. This is observed in the well-known prototypical Mn^{2+} -doped ZnS ($\text{ZnS}:\text{Mn}^{2+}$).³⁴ After the host ZnS nanoparticle is excited, energy can be transferred to excite the Mn^{2+} dopants present. Subsequently, radiative relaxation of the excited electrons can also occur through the Mn^{2+} dopants. This leads to a Mn^{2+} -related emission to be observed at ~ 585 nm in addition to the emissions originating from ZnS which usually occur in the ultraviolet and blue regions. Kar and Biswas even attempted to generate white light through the use of $\text{ZnS}:\text{Mn}^{2+}$ by having blue emission from ZnS, green emission from ZnO (oxidized surface of ZnS) and orange emission from Mn^{2+} dopants.³⁵

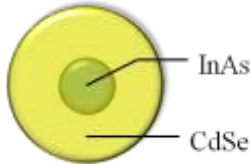
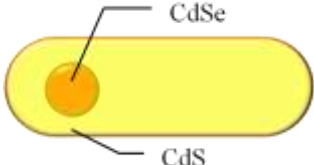
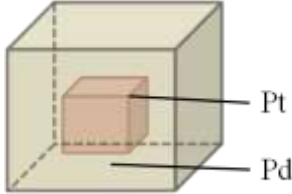

Dopants can also introduce magnetic properties into non-magnetic materials. Bogle et al.²⁹ had successfully realized magnetism by incorporating Co^{3+} into CdS nanocrystals. They also reported that the magnetic moment was dependent on the position of Co^{3+} dopants in the nanocrystals (interstitial or substitutional positions) and on its concentration present.

Despite the efforts spent on studying the doping behaviours of nanocrystals, doping remains a contentious topic in nanoscience. There were various dissimilar proposals to explain the range of doping efficiencies observed in nanocrystals of different materials. Dalpian and Chelikowsky³⁶ suggested smaller nanocrystals are harder to dope because of the higher formation energy required. Erwin *et al.*,³⁷ however, proposed that the types of surfaces present in the nanocrystals are important, even more so than the strength of interaction between dopants and capping agents. On the other hand, Du *et al.*³⁸ later proposed a model dependent on kinetically limited adsorption and desorption of dopants on nanoparticle surfaces. Essentially, nanocrystals are more easily doped if capping agents bind less strongly to the dopants compared to the adsorption of dopants on nanocrystals.

1.4.2 Heterostructured Nanocrystals

Heterostructured nanocrystals are formed when two or more materials of the same type are combined in one system and they could take various disparate forms such as: semiconductor-semiconductor core/shell (concentric core/shell³⁹ and seeded nanorods⁴⁰), metal-metal core/shell,⁴¹ metal-metal dimers.⁴² A schematic of these structures are presented in Table 1.1.

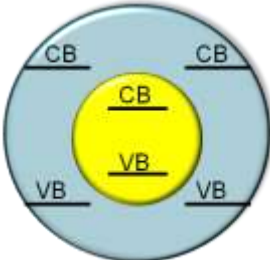
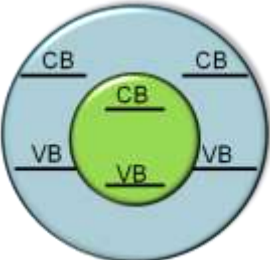
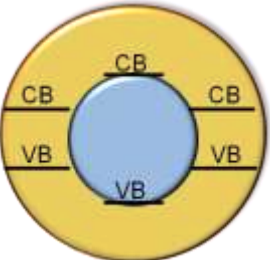
Table 1.1 Different morphologies of heterostructured nanocrystals synthesized in references 55-58.

Heterostructured Nanoparticle	Example
Semiconductor-semiconductor (concentric core/shell)	
Semiconductor-semiconductor (seeded nanorod)	
Metal-metal (core/shell)	
Metal-metal (dimers)	

Among these heterostructures, semiconductor-semiconductor core/shell nanocrystals have been extensively studied. Depending on the relative energy levels of the valance and conduction bands of the core and shell materials, such nanocrystals can be termed as either Type-I, Type-II or Reverse Type-I structures (Table 1.2).⁴³ For Type-I core/shell nanocrystals, the band gap of the core lies entirely within the band gap of the shell. The exciton pairs generated would be localized in the core and there may be a leakage of wave functions into the shell. The implication is that the band gap emission of the core is usually enhanced while at the same time red-shifted.⁴⁴ For Type-II core/shell nanocrystals, the valance and conduction bands of the

core and shell are staggered. A red shifted emission would be observed in this type of system because of the small resultant band gap between the lower conduction band and the higher valence band of the two materials present. The emission quantum efficiency is also expectedly low as it involves an indirect band gap relaxation.⁴⁵ Reverse Type-I nanocrystals, where band gap of the shell lies entirely within the band gap of the core, are also expected to have significant red shifted emission because the electron wave functions would be drastically leaked into the shell. Barring the comparatively low quantum efficiency, the study of Reverse Type-I systems is driven by the desire to understand the system at a fundamental level. CdS/CdSe⁴⁶ and ZnSe/CdSe⁴⁷ are some examples of such systems studied.

Table 1.2 Different types of semiconductor-semiconductor nanocrystals as illustrated using concentric core/shell nanocrystals. In all the diagrams, VB represents valance band and CB represents conduction band.

Type of core/shell nanoparticle		
Type-I	Type-II	Reverse Type-I
		

Metal-metal heterostructured nanocrystals had been associated with changes in catalytic, optical and magnetic properties. For example, Au-Ag alloy nanocrystals had been proven to have higher catalytic activities for the oxidation of CO in spite of their

larger size than pure Au nanocrystals. This has been attributed to the synergistic effect of the two noble metals present.⁴⁸

1.4.3 Hybrid Nanocrystals

Hybrid nanocrystals of different combination of materials and morphologies have also been studied in the literature. In these particles, two or more materials of different types are combined in one system. The attractiveness of such nanocrystals lies in their multi-functionalities. Recently, Fe₃O₄/Au and Fe₃O₄/Au/Ag core/shell nanocrystals have been reported to display great potentials in diagnostic applications owing to their magneto-optical properties and tunable plasmonic absorption by adjusting the composition of the shell.⁴⁹

Unlike the single-material nanocrystals, the synthesis mechanism and fundamentals of hybrid nanocrystals are less well-understood, even as sophisticated structures such as the Au with CdSe- arm nanotetrapods are synthesized.⁵⁰

The lack of understanding can be seen from the discrepancies in the observations of the synthesis of Au-decorated Type-I seeded nanorod. Menagen *et al.*⁵¹ and Yoskovitz *et al.*⁵² previously reported that Au nanocrystals grew selectively near the positions of the quantum dots in seeded nanorods (structure refers to *Table 1.1*) as the seeds acted as electron sinks providing electrons for the reduction of cationic gold precursors to gold. In contrast, nanorod tip-selective growth of Au nanocrystals had also been reported⁵³ and explained to be due to the high surface energy at the tips. It was further elaborated that of the two tips of the nanorods, the one which was sulfur-rich, hence negatively polarized and less passivated with the nucleophilic capping agents, would be the more preferable growth site of Au

nanoparticle.⁵³ Interestingly, there had also been instances when Au nanocrystals were randomly found along the nanorods^{51,54} and that was possibly due to a higher density of surface defects which acted as high surface energy nucleation sites.⁵⁵

1.5 Synthetic Methodologies of Nanocrystals

Nanocrystals can be obtained via either top-down or bottom-up approaches. In top-down approaches, nanocrystals are derived from larger materials. Lee *et al.*⁵⁶ and Hanada *et al.*⁵⁷ have demonstrated the use of milling, an example of top-down approach, in obtaining Fe₂O₃ and MgH₂ nanocrystals respectively. On the other hand, bottom-up approaches make use of the aggregation of molecular and atomic species to form nanocrystals. This type of approach relies predominantly on the chemical interactions between reactants used, which in turn offer room for a vast range of attainable nanocrystals. All methods employed in this thesis follow the bottom-up approach and the principles behind the chemical growth of particles would be elaborated in the following.

LaMer and Dinegar⁵⁸ developed a quintessential description for the crystallization of particles that could be broken down into the following phases (*Figure 1.1*): achieving supersaturation of reactants, homogeneous nucleation and growth of particles. Supersaturation is condition whereby the solute concentration has exceeded its solubility (nucleation concentration) and hence brought about nucleation. After this, the reactants form monomers thus giving rise to nanoparticle nuclei. Nuclei that are larger than a critical size would undergo further growth and continue to increase in size. The driving force behind such a growth is the lowering of free energy which is given by the sum of free energy consequential of new volume and surface

formed. It should be noted that nucleation ceases when the concentration of reactants fall below the supersaturation level and that would lead to two possible scenarios: (1) If there are still reactants present, size-focusing would occur for the nuclei formed. The driving force for the growth of smaller nuclei (that exceeds the critical size) is larger than that of larger nuclei due to the minimizing of surface area hence surface energy. (2) If the reactants are depleted, the larger nuclei would grow at the expense of the smaller nuclei in a phenomenon known as Ostwald ripening. A typical strategy in ensuring size uniformity of particles formed would be to shorten the nucleation period whereby all the nuclei are formed at around the same point in time and to suppress any secondary nucleation.¹¹

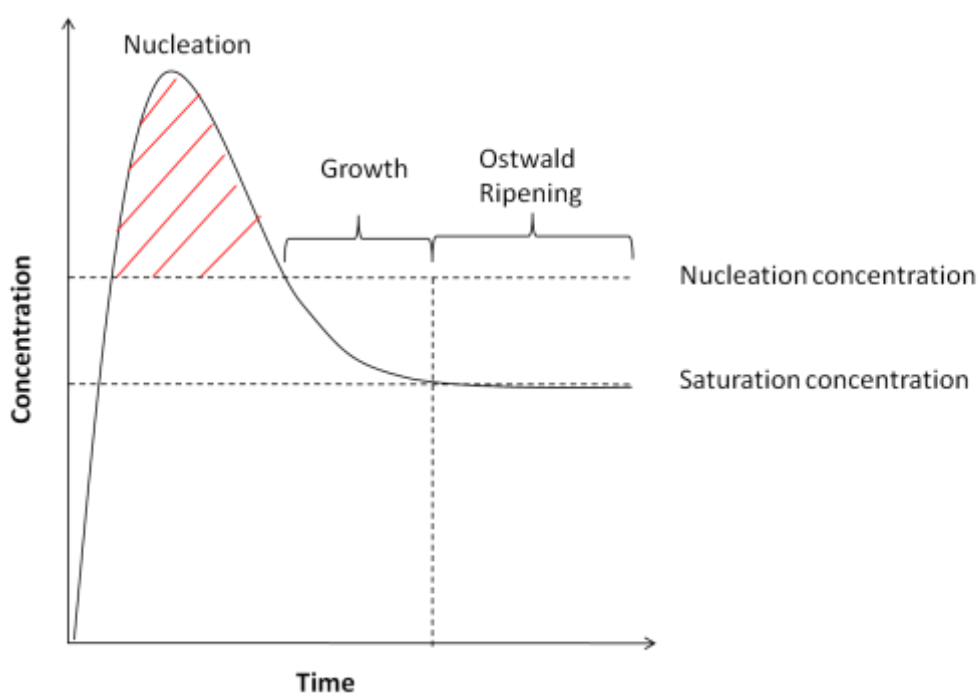


Figure 1.1 A plot showing crystallization process as described by LaMer and Dinegar. Nucleation occurs in the time period represented by the shaded region.

There is a variety of chemical methods available to synthesize nanocrystals and all of them have a common requirement in terms of the materials needed: precursors for the nanocrystals, capping agents to control the sizes of nanocrystals, and solvents. It should be noted that it is not uncommon for a reagent to play more than one role, for example, capping agents may act as solvents too.

Hereinafter, solution synthesis of nanocrystals would be briefly reviewed as it is the method of choice in the subsequent chapters.

1.5.1 Solution Synthesis of Nanocrystals

All the syntheses reported in this thesis were based on solution method. Solution method can be divided into two types: one-pot or two-pot reaction. In a one-pot reaction, all the necessary reagents are placed in one reaction vessel before the temperature is ramped up to the desired value. This method of synthesis appears to be simple in execution but a very stringent control over the temperature has to be exercised to ensure that the nanocrystals formed are uniformly sized. It is also necessary to ensure that rate of formation of monomers is slower than the addition of monomers to the nuclei for growth. Amongst others, Fe⁵⁹, Au⁶⁰ and Fe₃O₄⁶¹ nanocrystals have been synthesized using such one-pot method.

In a typical two-pot synthesis, there is one vessel that contains the precursor and another that contains the capping agent and a second precursor (if any). The precursor is then rapidly injected into vessel containing the capping agent after it is raised to the desired temperature. The injection has to be carried out rapidly to ensure a short nucleation period to achieve size mono-dispersity of the nanocrystals. This method offers a greater and easier control over its one-pot counterpart and its

popularity and versatility can be seen by its application to obtain less commonly studied nanoparticle systems like Ge⁶², Cu₂S⁶³ and In₂S₃⁶³.

1.5.2. Synthesis of Doped Nanocrystals

There are two commonly employed strategies in the solution syntheses of doped nanocrystals: growth doping and nucleation doping.

In growth doping, the dopant precursors are mixed together with the precursors for the host nanocrystals during syntheses. Other than the factors covered under Section 1.4.1, it is also important that all the precursors are miscible in a common solvent. Common dopant precursors are metal acetates and metal chlorides, including Mn(OAc)₂·4H₂O, Cu(OAc)₂·H₂O and EuCl₃.^{64,65} The products from such synthetic strategy would typically have the dopants incorporated into the lattice of the host or be residing on the host surfaces.

Nucleation doping strategy could be explained by considering the steps taken by Pradhan and Peng⁶⁶ in synthesizing ZnSe:Mn. Firstly, they synthesized MnSe nanocrystals. Then, they overcoated the MnSe nanocrystals with a ZnSe layer to achieve the desired products of ZnSe:Mn. Temperature was a crucial factor in determining the extent of mixing of the cations, Zn²⁺ and Mn²⁺. When a low temperature was used, the final nanocrystals had structures resembling the typical core/shell nanocrystals. On the other hand, when a high temperature was used, there would be an alloy layer formed at the interface of the MnSe core and the ZnSe shell hence attaining nanocrystals that resembled more closely to those that are obtained via growth doping.

1.5.3 Synthesis of Heterostructured and Hybrid Nanocrystals

In contrast to the synthesis of single-component nanocrystals where homogeneous nucleation occurs, the synthesis of heterostructured and hybrid nanocrystals concerns with heterogeneous nucleation. In this synthetic strategy, pre-formed particles of the first material are present together with the precursors of the second material. The synthesis conditions are maintained such that the precursor concentration of the second material and the reaction temperature are lower than that needed for homogeneous nucleation, thereby facilitating the nucleation of the second material onto the pre-formed particles. Moreover, the activation energy necessary for nucleating on pre-formed particles is also lower than if the precursors were to form new particles.⁶⁷

The key aspects in ensuring a success of heterogeneous nucleation include: capping agents used for pre-formed particles, quality of pre-formed particles and lattice mismatch between the materials.

The extent of steric hindrance provided by capping agents will directly affect the availability of surfaces on the pre-formed particles and hence the ease of heterogeneous nucleation. Casavola *et al.*⁶⁸ have recently demonstrated how manipulation of capping agent concentrations can result in site-selective deposition of magnetic Co nanocrystals onto TiO₂ nanorods to obtain hybrid nanocrystals. A low capping agent concentration would result in random Co depositions along the TiO₂ nanorods; a high capping agent concentration would favour tip-selective Co depositions on TiO₂ nanorods.

Quality of pre-formed particles is seen by their crystallinity which would affect the positions at which heterogeneous nucleation would occur. It could be

inferred that the pre-formed particles with poorer crystallinity would have a higher density of defects which are preferable sites for heterogeneous nucleation⁵³ due to their higher surface energies.

Lastly, heterogeneous nucleation would be favorable when the lattice mismatch between the materials in direct contact is small and there is small lattice strain. Talapin *et al.*⁶⁹ synthesized CdSe/CdS/ZnS and CdSe/ZnSe/ZnS where the centre materials, i.e. CdS and ZnSe respectively, had the role of mediating the lattice mismatch between the CdS core and the ZnS shell.

1.6 Objective and Scope of the Thesis

This project was undertaken with the aim to better understand hybrid, heterostructured and doped nanocrystals. During the process, the syntheses results were compared with previously reported results and new methods were developed.

The experimental details, in terms of reagents used and procedures, are described in Chapter 2.

In Chapter 3, we present the results of our work on sandwiched CdS|CdSe|CdS and CdSe|CdS|CdSe nanorods as well as a study the deposition of Au on these heterostructured sandwich nanorods. We noted that there had been a stark non-coherence in the observation and explanation in the literature on the deposition of Au on seeded nanorods (Section 1.4.3). We thus designed a series of experiments to investigate the deposition to ascertain if there is any form of selectivity towards the materials and/or the structures of the nanocrystals acting as deposition sites. By using the sandwiched structures instead of the prototypical seeded nanorod structures, we demonstrated that there is no preferential selectivity of Au deposition onto the low

band gap CdSe segments. On top of that, we also performed a temporal monitoring of the optical properties of the Au-deposited nanorods and revealed that the optical behavior has been altered with the deposition of Au.

Chapter 4 comprised of our work on nanocrystals of various types ranging from the single-component nanoparticle (CdS), heterostructured seeded nanorod (CdS/ZnS), heterostructured doped-and-seeded nanorod (CdS/ZnS:Mn²⁺) and lastly to the hybrid heterostructured nanoparticle (Au-CdS/ZnS:Mn²⁺). The motivation for this piece of work was two-fold. Firstly, it was to present a systematic step-by-step synthesis of these different types of nanocrystals. The second motivation was to probe the changes in optical properties of the structures systematically altered. By doing so, we could also investigate the interactions between different materials when they were combined into one complex system.

The methodology details of our experiments are given in Chapter 2, while an overall conclusion is summarized and some future outlooks for the project are given in Chapter 5.

1.7 References

- (1) Colvin, V. L.; Schlamp, M. C.; Alivisatos, A. P. *Nature* **1994**, *370*, 4.
- (2) Alivisatos, A. P.; Gu, W.; Larabell, C. *Annu. Rev. Biomed. Eng.* **2005**, *7*, 26.
- (3) Bruchez Jr., M.; Moronne, M.; Gin, P.; Weiss, S.; Alivisatos, A. P. *Science* **1998**, *281*, 4.
- (4) Ahrenkiel, S. P.; Micic, O. I.; Miedaner, A.; Curtis, C. J.; Nedeljkovic, J. M.; Nozik, A. J. *Nano. Lett.* **2003**, *3*, 5.
- (5) Micic, O. I.; Curtis, C. J.; Jones, K. M.; Sprague, J. R.; Nozik, A. J. *J. Phys. Chem.* **1994**, *98*, 4.

-
- (6) Ramvall, P.; Tanaka, S.; Nomura, S.; Riblet, P.; Aoyagi, Y. *Appl. Phys. Lett.* **1998**, *73*, 3.
 - (7) Sau, T. K.; Murphy, C. J. *J. Am. Chem. Soc.* **2004**, *126*, 2.
 - (8) Xie, J.; Zhang, Q.; Lee, J. Y.; Wang, D. I. C. *ACS Nano* **2008**, *2*, 8.
 - (9) Ohde, H.; Hunt, F.; Wai, C. M. *Chem. Mater.* **2001**, *13*, 6.
 - (10) Maillard, M.; Huang, P.; Brus, L. *Nano. Lett.* **2003**, *3*, 5.
 - (11) Murray, C. B.; Norris, D. J.; Bawendi, M. G. *J. Am. Chem. Soc.* **1993**, *115*, 10.
 - (12) Leatherdale, C. A.; Woo, W.-K.; Mikulec, F. V.; Bawendi, M. G. *J. Phys. Chem. B* **2002**, *106*, 4.
 - (13) Mittleman, D. M.; Schoenlein, R. W.; Shiang, J. J.; Colvin, V. L.; Alivisatos, A. P.; Shank, C. V. *Phys. Rev. B* **1994**, *49*, 12.
 - (14) Bowers II, M. J.; McBride, J. R.; Rosenthal, S. J. *J. Am. Chem. Soc.* **2005**, *127*, 2.
 - (15) Peng, Z. A.; Peng, X. *J. Am. Chem. Soc.* **2002**, *124*, 11.
 - (16) Goldstein, A. N.; Echer, C. M.; Alivisatos, A. P. *Science* **1992**, *256*, 3.
 - (17) Link, S.; El-Sayed, M. A. *Int. Rev. Phys. Chem.* **2000**, *19*, 46.
 - (18) Hostetler, M. J.; Wingate, J. E.; Zhong, C.-J.; Harris, J. E.; Vachet, R. W.; Clark, M. R.; Londono, J. D.; Green, S. J.; Stokes, J. J.; Wignall, G. D.; Glish, G. L.; Porter, M. D.; Evans, N. D.; Murray, R. W. *Langmuir* **1998**, *14*, 14.
 - (19) Narayanan, R.; El-Sayed, M. A. *Nano. Lett.* **2004**, *4*, 6.
 - (20) Mostafa, S.; Behafarid, F.; Croy, J. R.; Ono, L. K.; Li, L.; Yang, J. C.; Frenkel, A. I.; Cuenya, B. R. *J. Am. Chem. Soc.* **2010**, *132*, 6.
 - (21) Hu, J.; Li, L.-S.; Yang, W.; Manna, L.; Wang, L.-W.; Alivisatos, A. P. *Science* **2001**, *292*, 5.
 - (22) Lee, S.-M.; Cho, S.-N.; Cheon, J. *Adv. Mater.* **2003**, *15*, 4.
 - (23) Zelaya-Angel, O.; Alvarado-Gil, J. J.; Lozada-Morales, R.; Vargas, H.; da Silva, A. F. *Appl. Phys. Lett.* **1994**, *64*, 3.
 - (24) Kim, F.; Song, J. H.; Yang, P. *J. Am. Chem. Soc.* **2002**, *124*, 2.
 - (25) Vassilieff, T.; Sutton, A.; Kakkar, A. K. *J. Mater. Chem.* **2008**, *18*, 3.

-
- (26) Jana, N. R.; Gearheart, L.; Murphy, C. J. *Chem. Commun.* **2001**, 2.
- (27) Yu, H.; Chen, M.; Rice, P. M.; Wang, S. X.; White, R. L.; Sun, S. *Nano. Lett.* **2005**, 5, 4.
- (28) Nag, A.; Chakraborty, S.; Sarma, D. D. *J. Am. Chem. Soc.* **2008**, 130, 7.
- (29) Bogle, K. A.; Ghosh, S.; Dhole, S. D.; Bhoraskar, V. N.; Fu, L.; Chi, M.; Browning, N. D.; Kundaliya, D.; Das, G. P.; Ogale, S. B. *Chem. Mater.* **2008**, 20, 7.
- (30) Radovanovic, P. V.; Gamelin, D. R. *J. Am. Chem. Soc.* **2001**, 123, 8.
- (31) Norris, D. J.; Yao, N.; Charnok, F. T.; Kennedy, T. A. *Nano. Lett.* **2001**, 1, 7.
- (32) Pradhan, N.; Goorskey, D.; Thessing, J.; Peng, X. *J. Am. Chem. Soc.* **2005**, 127, 2.
- (33) Bol, A. A.; van Beek, R.; Meijerink, A. *Chem. Mater.* **2002**, 14, 7.
- (34) Bhargava, R. N.; Gallagher, D. *Phys. Rev. Lett.* **1994**, 72, 4.
- (35) Kar, S.; Biswas, S. *J. Phys. Chem. C* **2008**, 112, 6.
- (36) Dalpian, G. M.; Chelikowsky, J. R. *Phys. Rev. Lett.* **2006**, 96, 4.
- (37) Erwin, S. C.; Zu, L.; Haftel, M. I.; Efros, A. L.; Kennedy, T. A.; Norris, D. J. *Nature* **2005**, 436, 4.
- (38) Du, M.-H.; Erwin, S. C.; Efros, A. L. *Nano. Lett.* **2008**, 8, 6.
- (39) Cao, Y.; Banin, U. *J. Am. Chem. Soc.* **2000**, 122, 11.
- (40) Carbone, L.; Nobile, C.; De Giorgi, M.; Sala, F. D.; Morello, G.; Pompa, P.; Hych, M.; Snoeck, E.; Fiore, A.; Franchini, I. R.; Nadasan, M.; Silvestre, A. F.; Chiodo, L.; Kudera, S.; Cingolani, R.; Krahne, R.; Manna, L. *Nano. Lett.* **2007**, 7, 9.
- (41) Habas, S. E.; Lee, H.; Radmilovic, V.; Somorjai, G. A.; Yang, P. *Nature Mater.* **2007**, 6, 6.
- (42) Sheikholeslami, S.; Jun, Y.-W.; Jain, P. K.; Alivisatos, A. P. *Nano. Lett.* **2010**, 10, 6.
- (43) Reiss, P.; Protiere, M.; Li, L. *Small* **2009**, 5, 15.
-

-
- (44) Steckel, J. S.; Zimmer, J. P.; Coe-Sullivan, S.; Stott, N. E.; Bulovic, V.; Bawendi, M. G. *Angew. Chem. Int. Ed.* **2004**, *43*, 5.
- (45) Steiner, D.; Dorfs, D.; Banin, U.; Sala, F. D.; Manna, L.; Millo, O. *Nano. Lett.* **2008**, *8*, 5.
- (46) Battaglia, D.; Li, J. J.; Wang, Y. J.; Peng, X. *Angew. Chem. Int. Ed.* **2003**, *42*, 5.
- (47) Zhong, X.; Xie, R.; Zhang, Y.; Basche, T.; Knoll, W. *Chem. Mater.* **2005**, *17*, 5.
- (48) Liu, J.-H.; Wang, A.-Q.; Chi, Y.-S.; Lin, H.-P.; Mou, C.-Y. *J. Phys. Chem. B* **2005**, *109*, 4.
- (49) Xu, Z.; Hou, Y.; Sun, S. *J. Am. Chem. Soc.* **2007**, *129*, 2.
- (50) Yong, K.-T.; Sahoo, Y.; Swihart, M. T.; Prasad, P. N. *Adv. Mater.* **2006**, *18*, 5.
- (51) Menagen, G.; Mocatta, D.; Salant, A.; Popov, I.; Dorfs, D.; Banin, U. *Chem. Mater.* **2008**, *20*, 3.
- (52) Yoskovitz, E.; Menagen, G.; Sitt, A.; Lachman, E.; Banin, U. *Nano. Lett.* **2010**, *10*, 5.
- (53) Menagen, G.; Macdonald, J. E.; Shemesh, Y.; Popov, I.; Banin, U. *J. Am. Chem. Soc.* **2009**, *131*, 6.
- (54) Chakraborty, S.; Yang, J. A.; Tan, Y. M.; Mishra, N.; Chan, Y. *Angew. Chem. Int. Ed.* **2010**, *49*, 5.
- (55) Saunders, A. E.; Popov, I.; Banin, U. *J. Phys. Chem. B* **2006**, *110*, 9.
- (56) Lee, C.-S.; Lee, J.-S.; Oh, S.-T. *Mater. Lett.* **2003**, *57*, 4.
- (57) Hanada, N.; Ichikawa, T.; Fujii, H. *J. Phys. Chem. B* **2005**, *109*, 7.
- (58) LaMer, V. K.; Dinegar, R. H. *J. Am. Chem. Soc.* **1950**, *72*, 8.
- (59) Peng, S.; Wang, C.; Xie, J.; Sun, S. *J. Am. Chem. Soc.* **2006**, *128*, 2.
- (60) Dong, H.; Zhu, M.; Yoon, J. A.; Gao, H.; Jin, R.; Matyjaszewski, K. *J. Am. Chem. Soc.* **2008**, *130*, 2.
- (61) Li, Z.; Chen, H.; Bao, H.; Gao, M. *Chem. Mater.* **2004**, *16*, 3.
- (62) Ruddy, D. A.; Johnson, J. C.; Smith, E. R.; Neale, N. R. *ACS Nano* **2010**, *4*, 8.
-

- (63) Han, W.; Yi, L.; Zhao, N.; Tang, A.; Gao, M.; Tang, Z. *J. Am. Chem. Soc.* **2008**, *130*, 10.
- (64) Sun, L.; Yan, C.; Liu, C.; Liao, C.; Li, D.; Yu, J. *J. Alloys. Compd.* **1998**, *275*, 4.
- (65) Karan, N. S.; Sarma, D. D.; Kadam, R. M.; Pradhan, N. *J. Phys. Chem. Lett.* **2010**, *1*, 4.
- (66) Pradhan, N.; Peng, X. *J. Am. Chem. Soc.* **2007**, *129*, 9.
- (67) Casavola, M.; Buonsanti, R.; Caputo, G.; Cozzoli, P. D. *Eur. J. Inorg. Chem.* **2008**, 18.
- (68) Casavola, M.; Grillo, V.; Carlino, E.; Giannini, C.; Gozzo, F.; Pinel, E. F.; Garcia, M. A.; Manna, L.; Cingolani, R.; Cozzoli, P. D. *Nano. Lett.* **2007**, *7*, 10.
- (69) Talapin, D. V.; Mekis, I.; Gotzinger, S.; Kornowski, A.; Benson, O.; Weller, H. *J. Phys. Chem. B* **2004**, *108*, 6.

Chapter 2

Experimental

2.1 Chemical reagents

All chemicals listed in Table 2.1 are obtained commercially and used as-received, unless otherwise stated.

Table 2.1 Chemicals and solvents used and their respective percentage purities and sources.

Chemical	Purity / %	Formula	Source
Trioctylphosphine (TOP)	~ 90	$[\text{CH}_3(\text{CH}_2)_7]_3\text{P}$	Aldrich
Gold (III) Chloride	99.99	AuCl_3	Aldrich
Cetyltrimethylammonium Bromide (CTAB)	99	$[\text{CH}_3(\text{CH}_2)_{15}\text{N}(\text{CH}_3)]_3\text{Br}$	Aldrich
Sodium Carbonate Decahydrate	95	$\text{Na}_2\text{CO}_3 \cdot 10\text{H}_2\text{O}$	Dumont
Thiobenzoic Acid (TBA)	90	$\text{C}_6\text{H}_5\text{COSH}$	Fluka
Manganese Acetate Tetrahydrate	99	$\text{Mn}(\text{CH}_3\text{COO})_2 \cdot 4\text{H}_2\text{O}$	Fluka
Cadmium Oxide	99.95	CdO	Alfa Aesar
Sulfur Sublimed	99.65	S	Chemicon
Selenium Metal	99.9	Se	Fluka
1-Tetradecylphosphonic Acid (TDPA)	98	$\text{CH}_3(\text{CH}_2)_{13}\text{PO}(\text{OH})_2$	Alfa Aesar
Trioctylphosphine Oxide (TOPO)	99	$[\text{CH}_3(\text{CH}_2)_7]\text{PO}$	Aldrich
1-Hexadecylamine (HDA)	98	$\text{CH}_3(\text{CH}_2)_{15}\text{NH}_2$	Aldrich
Dodecylamine (DDA)	98	$\text{CH}_3(\text{CH}_2)_{11}\text{NH}_2$	Aldrich
Oleylamine (OLA)	70	$\text{CH}_3(\text{CH}_2)_7\text{CH}=\text{CH}(\text{CH}_2)_8\text{NH}_2$	Aldrich
Cadmium Chloride	98	$\text{CdCl}_2 \cdot 2\frac{1}{2}\text{H}_2\text{O}$	Nacalai Tesque
Zinc Chloride	98	ZnCl_2	Riedel-de-Haen
Hexane	95	$\text{CH}_3(\text{CH}_2)_4\text{CH}_3$	Tedia
Ethanol	AR grade	$\text{CH}_3\text{CH}_2\text{OH}$	Fisher Scientific

2.2 Preparation procedures

2.2.1 Preparation of CdS|CdSe|CdS nanorods

The sandwiched CdS|CdSe|CdS nanorods were synthesized following a method previously reported by Korgel *et al.*³ The Cd precursor was prepared in a 25-mL three-necked round-bottom flask (RBF), where 0.0285 g ($\sim 2.22 \times 10^{-4}$ mol) CdO, 0.1075 g ($\sim 3.86 \times 10^{-4}$ mol) 1-tetradecylphosphonic acid (TDPA) and 1.7500 g ($\sim 4.53 \times 10^{-3}$ mol) trioctylphosphine oxide (TOPO) were mixed and warmed to 65 °C. Then, the mixture was degassed for 3 hours at 65 °C. After degassing, the temperature of the mixture was raised to 340 °C for 10 minutes and the temperature was subsequently brought down to 260 °C. The mixture was noted to change from dark red to colourless at ~ 300 °C. Se and S precursors were prepared by having 0.0197 g ($\sim 2.49 \times 10^{-4}$ mol) Se and 0.0080 g ($\sim 2.49 \times 10^{-4}$ mol) S dissolved in 1.250 mL ($\sim 2.80 \times 10^{-3}$ mol) TOP in two separate 25-mL two-necked RBFs and heated to 120 °C. Following that, the Se precursor was injected into the flask containing the Cd precursor. Four injections (0.12 mL per injection) were made with a three-minute interval between successive injections. The temperature of the flask containing the Cd precursor was then raised to 300 °C. After which, the S precursor was injected eight times (0.12 mL per injection). Each injection of the S precursor was separated by a two-minute interval. After all the injections were conducted, the reaction mixture was left to react for another 10 minutes before it was cooled to room temperature. The nanorods formed were first dispersed in hexane before they were re-precipitated using

ethanol. After washing, the nanorods were dispersed in hexane, and kept in a sample vial, under an inert gas atmosphere.

2.2.2 Preparation of CdSe|CdS|CdSe nanorods

The steps taken were as described under Section 2.2.1 except that the S precursor was injected before the Se precursor.

2.2.3 Preparation of gold-deposited CdS|CdSe|CdS and CdSe|CdS|CdSe nanorods

Au nanoparticles were deposited onto the CdS|CdSe|CdS and CdSe|CdS|CdSe sandwiched nanorods using the method described by Menagen *et al.*³ The CdS|CdSe|CdS nanorods (~ 0.18 mM) synthesized in Section 2.2.1, together with 3 mL hexane, were first placed in a 25-mL three-necked RBF and warmed to 40 °C. In a separate 25-mL two-necked round-bottom flask, 0.0197 g (~ 5.40 x 10⁻⁵ mol) cetyltrimethylammonium bromide (CTAB), 50 µL (~ 2.17 x 10⁻⁴ mol) dodecylamine (DDA) and 0.0168 g (~ 5.54 x 10⁻⁵ mol) AuCl₃ were dissolved in 2.45 mL hexane and the mixture was sonicated for 15 minutes, during which a colour change from orange to yellow was observed. Next, the mixture was vigorously stirred for 30 minutes and warmed at 40 °C for 5 minutes. This mixture was then rapidly injected into the flask

containing the CdS|CdSe|CdS nanorods and was allowed to stir for 10 minutes at 40 °C. Ethanol was added to precipitate the products.

The same procedures were followed to deposit Au nanoparticles on CdSe|CdS|CdSe nanorods.

2.2.4 Preparation of cadmium thiobenzoate and zinc thiobenzoate precursors

Both cadmium thiobenzoate (CdTB) and zinc thiobenzoate (ZnTB) were prepared following a method reported by Savent *et al.*¹ For the preparation of CdTB, 2.3 g ($\sim 1.00 \times 10^{-2}$ mol) CdCl₂.2½ H₂O was first dissolved in 20 mL deionised water. In a separate flask, 2.9 g ($\sim 1.00 \times 10^{-2}$ mol) of Na₂CO₃.10H₂O was dissolved in 20 mL deionised water and added with 2.4 mL ($\sim 2.03 \times 10^{-2}$ mol) thiobenzoic acid (TBA). The resultant mixture was allowed to stir for a period of 30 min before it was added to the stirring CdCl₂ solution in a dropwise manner. After which, the reaction was left at room temperature with string for an hour. The cream-coloured precipitate formed was isolated, dispersed using hexane and re-precipitated using deionised water. It was then centrifuged and dried under vacuum in the presence of the drying agent phosphorus (V) oxide.

The same procedure was followed for the preparation of ZnTB, except that CdCl₂.2½ H₂O was replaced by ZnCl₂.

2.2.5 Preparation of CdS quantum dots

0.0800 g ($\sim 2.07 \times 10^{-4}$ mol) CdTB prepared in Section 2.2.4 was first dissolved in 0.4 mL ($\sim 8.99 \times 10^{-4}$ mol) trioctylphosphine (TOP) in a 25-mL 3-necked RBF and degassed at 60 °C. In another 25-mL 3-necked RBF, 0.9988 g ($\sim 4.14 \times 10^{-3}$ mol) hexadecylamine (HDA) was degassed also at 60 °C and raised to 120 °C after 20 minutes of degassing. The whole amount of CdTB solution was then rapidly injected into the hot solution of HDA and the reaction mixture was left at 120 °C for 10 minutes. After cooling down to room temperature, the CdS quantum dots formed were first dispersed in hexane and re-precipitated in ethanol, and subsequently centrifuged and dried overnight under vacuum.

2.2.6 Preparation of CdS-seeded Mn²⁺-doped ZnS

Dried sample of 0.0007 g CdS prepared in Section 2.2.5 was first sonicated in 2.00 mL hexane placed in a 25-mL 3-necked RBF for 15 minutes. After which, 0.1645 g ($\sim 4.84 \times 10^{-4}$ mol) ZnTB, 0.0012 g ($\sim 4.89 \times 10^{-6}$ mol) C₄H₆MnO₄·4H₂O and 12.75 mL ($\sim 3.88 \times 10^{-2}$ mol) OLA were added to the mixture and the procedures as described in Section 2.2.5 were followed.

2.2.7 Preparation of gold-decorated CdS-seeded Mn²⁺-doped ZnS

The procedures taken were similar to that described under Section 2.2.3 with CdS/ZnS:Mn²⁺ used instead of the sandwiched nanorods.

2.3 Characterisation Techniques

2.3.1 Transmission Electron Microscopy and High Resolution Transmission Electron Microscopy

Transmission electron microscopy (TEM) is analogous to light microscopy, with the difference in the use of an electron beam instead of a light source. Unscattered electrons that pass through a sample will be captured on a fluorescent screen resulting in the image. The use of TEM is advantageous because of the shorter electron de Broglie wavelength that makes it possible for samples to be defined with a higher degree of resolution.

In this work, TEM analysis was performed using a JOEL 2010 microscope with an accelerating voltage of 200 kV while high resolution TEM (HRTEM) was performed using JOEL 3010 microscope with an accelerating voltage of 300 kV. Both TEM and HRTEM were used for characterising the morphologies and dimensions of the nanoparticles. The samples to be characterised were first dispersed in hexane and one drop of the nanoparticle solution was dripped onto a 200- or 400-mesh carbon-coated copper grid. All the grids prepared were dried in vacuum before analysis.

2.3.2 Ultraviolet-visible Absorption Spectroscopy

Spectroscopy broadly refers to techniques that involve the interaction of matters with light. Light in the ultraviolet-visible (UV-Vis) range provides sufficient energy for electronic transitions. Thus UV-Vis absorption spectroscopy can be used to probe the energy gaps between different electronic levels. When carrying out UV-Vis absorption spectroscopy, it is important to ensure that the samples are well-dispersed and are of sufficiently low concentrations. Scattering of the light source could occur if the samples are not well-dispersed while high concentrations of samples could result in changes of the refractive index.

All UV-Vis spectra reported here were collected with Shimadzu UV-3600 UV-VIS-NIR spectrophotometer. The reference used in all cases was pure hexane and all the nanoparticle samples were dispersed in pure hexane before analysis.

2.3.3 Steady-state Photoluminescence Spectroscopy

Photoluminescence (PL) is a spectroscopic technique that records the radiative relaxation of samples that are excited through irradiation. The excitation radiation used is typically slightly higher than the energy gap to be probed. Unlike the UV-Vis absorption spectroscopy, PL measurements are carried out without reference cell. It is often useful to interpret the information obtained from PL and UV-Vis absorption spectroscopies together.

PL spectra were collected at room temperature with a Jobin Yvon Fluorolog-3 modular spectrofluorometer using a 450 W xenon lamp source. All nanoparticle samples were dispersed in pure hexane and diluted to suitable concentrations, with absorbance at ~ 0.1 as determined from the UV-Vis spectra, before analysis.

2.3.4 Elemental Analysis

In carrying out elemental analysis (EA), the samples were first digested using a suitable acid (typically concentrated HNO_3). Subsequently, the samples were atomised and ionised with the use of argon plasma that was generated by electric current.

Inductively Coupled Plasma (ICP) analysis was performed using a Perkin-Elmer Optimer 5300 DV ICP-OES System.

2.3.5 Thermal Gravimetric Analysis

Thermal gravimetric analysis (TGA) monitors the change in weight of samples with respect to variation in temperature. The environment that the samples are heated in is typically purged with an inert gas to drive out gases (such as O_2) that may cause any undesirable side reactions.

TGA was conducted on a SDT 2960 simultaneous DTA-TGA analyzer. At least 5 mg of samples were placed in the instrument holder and readings were

recorded under a constant flow of nitrogen gas at a flow rate of 100 mL min⁻¹. The heating rate employed was 20 °C min⁻¹.

2.3.6 Powder X-Ray Diffraction

X-ray diffraction (XRD) is useful in fingerprint characterization of crystalline materials as well as for determining their phase information. Diffracted rays are generated from the interaction of X-rays with the lattice spacing of various crystal planes of the samples. The XRD patterns generated are plots of counts per second with respect to 2θ where the counts are signals converted from reflected X-ray, while θ describes the angle between the X-ray path and the samples.

Powder XRD patterns were obtained using a Siemens D5005 diffractometer using Cu K α radiation ($\lambda = 0.15406$ nm) with a scanning step of 0.01 ° and a step time of 1.5 s. The nanoparticle samples were prepared by grinding and placing on double-sided tapes that were mounted onto the sample holder.

2.4 References

- (1) Savant, V. V.; Gopalakrishnan, J.; Patel, C. C. *Inorg. Chem.* **1970**, *9*, 748.
- (2) Menagen, G.; Mocatta, D.; Salant, A.; Popov, I.; Dorfs, D.; Banin, U. *Chem. Mater.* **2008**, *20*, 6900.
- (3) Shieh, F.; Saunders, A. E.; Korgel, B. *J. Phys. Chem. B* **2005**, *109*, 8538.

Chapter 3

Gold Deposition on CdSe|CdS Heterostructured Sandwiched Nanorods

This piece of work was motivated by some controversies reported in the literature concerning heterostructured CdSe-CdS nanoparticles. Previous studies on the deposition of Au nanoparticles on the archetypal CdSe-seeded CdS nanorods had shown different conclusions as (i) to (iii) in the following: (i) Au nanoparticles were observed to be selective towards sites near the embedded CdSe seeds that were proposed to have acted as electron sinks.¹ (ii) On the other hand, tip-selective growth of Au nanoparticles was observed and attributed to the high surface energy at the tips of anisotropic nanoparticles.² (iii) Au nanoparticles were also observed to be randomly found along the nanorods,^{1,3} which were believed to have a high density of surface defects facilitating their roles as the nucleation sites.⁴

These discrepancies reported in the literature revealed the difficulties in the synthesis and precise engineering of nanoparticles that could allow proper accounting of various experimental observations. For example, the CdSe-seeded CdS nanorods may not be the best candidate to investigate Au deposition since the thickness of the CdS shell could make an important influence.¹

In this Chapter, we proposed to study the Au deposition on CdS|CdSe|CdS segmented nanorods (referred to as ABA nanorods) as well as its reversed structure, i.e. the CdSe|CdS|CdSe segmented nanorods (referred to as BAB nanorods). There were two reasons behind our choice of using such sandwiched nanorods in this work:

(1) The presence of sides with different surface energies and densities of surface defects allowed us to investigate if the Au deposition would occur preferentially at the higher surface energy region (tips) or the greater surface defects density region (sides) of the elongated nanorods. (2) Both CdSe and CdS were exposed to test if the Au deposition would show selectivity towards either of the two semiconductors of different band gaps.

In our study, we observed that Au deposition first occurred randomly along both the ABA and BAB nanorods suggesting defect growths regardless of material A or B. However, after an extended reaction period, Ostwald ripening possibly resulted in larger and more Au nanoparticles at the tips of the sandwiched nanostructures (*Section 3.3*). We also followed up our investigation with a temporal monitoring of the optical properties of the Au-deposited nanorods (*Section 3.4*) and found that the electronic structures of the nanorods might have been altered with the introduction of Au.

3.1 Synthesis and characterization of the CdS|CdSe|CdS and CdSe|CdS|CdSe sandwiched nanorods

Following the syntheses of both the CdS|CdSe|CdS (ABA) (*Figure 3.1a*) and CdSe|CdS|CdSe (BAB) (*Figure 3.1b*) segmented nanorods as described in *Section 2.2.1* and *Section 2.2.2*, TEM analysis was employed to confirm the morphology of the products. It was estimated from the respective TEM images in *Figure 3.2* that the ABA nanorods (*Figure 3.2a*) had an average length of 47.8 ± 4.1 nm and diameter of 6.8 ± 0.9 nm whereas the BAB nanorods (*Figure 3.2b*) had an average length of 32.7

± 4.2 nm and diameter of 3.6 ± 0.6 nm. Thus, both types of nanorods had an aspect ratio of $\sim 7:1$.



Figure 3.1. Cartoon illustration of (a) ABA and (b) BAB nanorods, where A denotes CdS and B denotes CdSe.

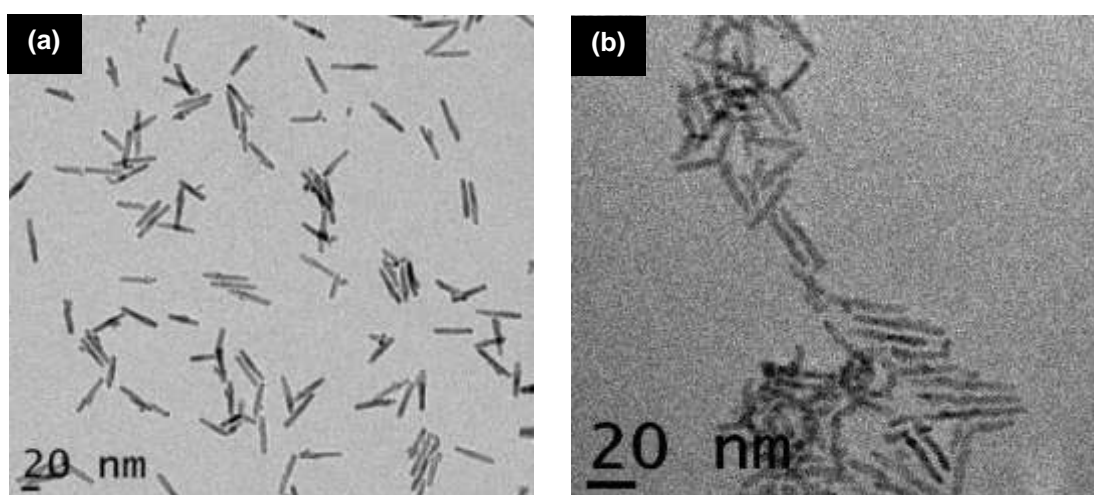


Figure 3.2. TEM images of the (a) ABA and (b) BAB nanorods, where A denotes CdS and B denotes CdSe.

The XRD diffraction patterns collected showed that both nanorods were of wurtzite phase, as clearly seen by the characteristic (110), (103) and (112) peaks in *Figure 3.3*. The use of a high reaction temperature was known to yield CdS and CdSe of wurtzite structures.⁵⁻⁷ From the narrow and sharp peaks, it could be deduced that there were minimal stacking faults along the nanorods. A comparison between the

XRD patterns with those of bulk CdS and CdSe revealed that the relative intensities of the patterns were different between the nanorods and the bulk materials. An enhancement of the (002) diffraction was evident in the nanorods, confirming an elongation associated with the (002) planes along the c -axis.⁸ Thus, not only did the XRD patterns characterize the wurzite structures of the nanorods, they further supported the nanorod morphology.

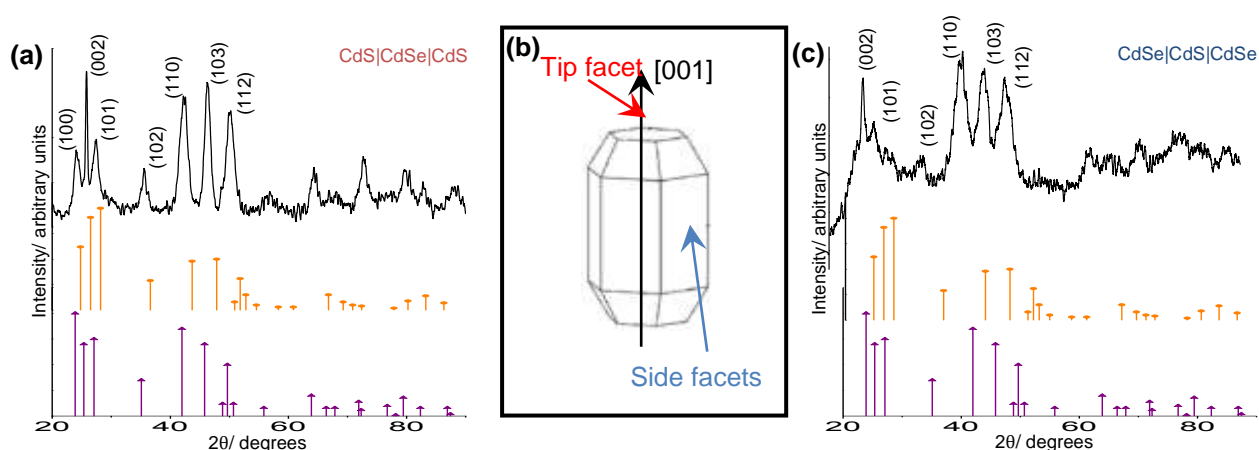


Figure 3.3. XRD patterns for the (a) ABA and (c) BAB nanorods indexed to the standard crystal patterns of CdS (orange, JCPDS 41-1409) and CdSe (purple, JCPDS 08-0459) respectively. (b) Schematic illustration of the wurzite crystal structure with its side and tip facets, and an arrow indicating the direction of growth along the [001] direction, corresponding to the unique c -axis of the wurzite structure.

The presence of a trioctylphosphine oxide – 1-tetradecylphosphonic acid (TOPO-TDPA) mixed surfactant system was instrumental in obtaining the desired nanorod morphology. It had been calculated⁹ from first principles that TOPO and TDPA had the ability to better bind to the sides of the nanorods as compared to the

tips of the nanorods, thus facilitating growth in the elongated direction. The importance of alkyl-phosphonic oxides and alkyl-phosphonic acids in the final morphology of nanoparticles had also been demonstrated experimentally.^{10,11} Interestingly, pure TOPO would not function well as capping agent alone for the growth of nanorods but would instead lead to uncontrollable growth into crystals of much larger dimensions. This is due to the three bulky alkyl chains attached to the P atom in TOPO (*Figure 3.4*) that would cause considerable steric hindrance and thereby greatly reducing the effectiveness of TOPO as capping agent. In some cases, a mixture of technical grade TOPO which contains other phosphonic organic compounds such as TDPA is used.^{9,10}

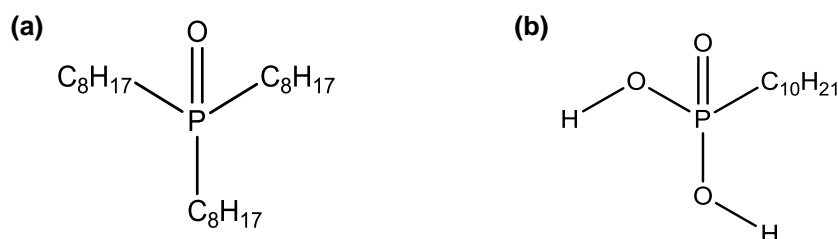


Figure 3.4. Chemical structures of (a) trioctylphosphine oxide and (b) 1-tetradecylphosphonic acid.

We made use of HRTEM to validate that segmented nanorods were synthesized instead of individual CdS and CdSe nanorods. From the HRTEM images shown in *Figure 3.5*, lattice planes of CdS (002) and CdSe (002) could be respectively identified on the two ends of the ABA and BAB sandwiched nanorods. Other the other hand, lattice planes of CdSe (002) and CdS (002) respectively are found at the middle segments of the two nanorods. Standard reference values in the database are CdS (002): 3.36 Å and CdSe (002): 3.51 Å.

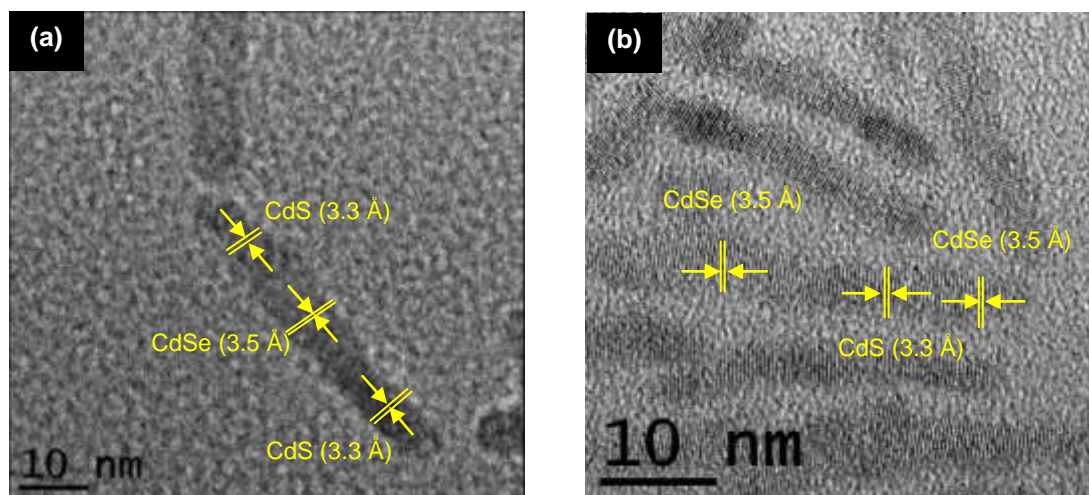


Figure 3.5. HRTEM images of (a) ABA and (b) BAB nanorods prepared. The *d*-spacings identified were 3.3 Å for CdS (002) and 3.5 Å for CdSe (002) in both (a) and (b).

3.2 Optical properties of the CdS|CdSe|CdS and CdSe|CdS|CdSe sandwiched nanostructures

In this section, we compared the optical properties of the sandwiched nanorods with that of the pure CdS nanorods, CdSe nanorods and a 1:1 physical mixture of CdS and CdSe nanorods. Figures 3.7a and 3.7b showed the PL peaks attributed to the band gaps emissions of CdS and CdSe nanorods at 450 nm and 565 nm respectively. Next, we prepared a 1:1 physical mixture of CdS and CdSe nanorods, by first adjusting the individual nanorods solution to the same concentrations using their UV-Vis absorbance values. Clearly, the spectrum in Figure 3.7c resembled a superposition of both the spectra in Figures 3.7a and 3.7b. This strongly suggested that the emissive properties of the CdS and CdSe nanorods remained highly characteristic of the

individual nanorods in a physical mixture. The result thus showed that there is no optically observable interaction between the two types of nanorods in the mixed sample.

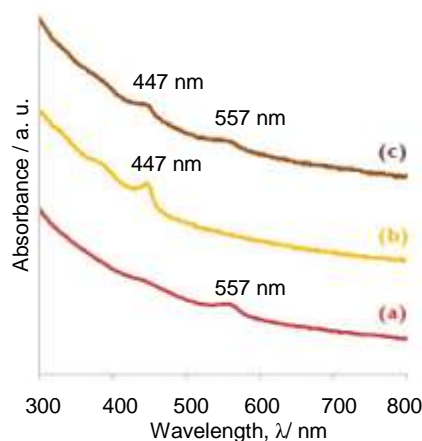


Figure 3.6. UV-Vis spectra of (a) pure CdSe, (b) pure CdS and (c) a 1:1 physical mixture of CdS and CdSe nanorods.

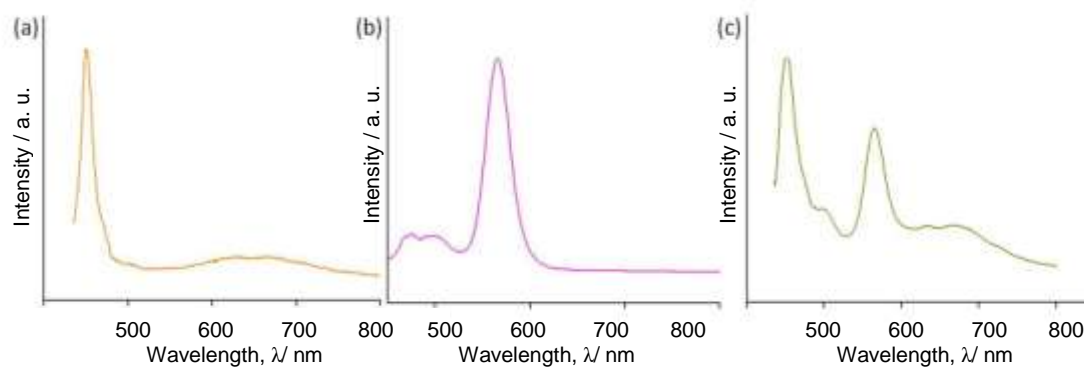


Figure 3.7. PL spectra ($\lambda_{excitation} = 420$ nm) of (a) CdS, (b) CdSe and (c) a 1:1 physical mixture of CdS and CdSe nanorods. The broad peak in spectra (a) and (c) from ~ 550 nm to ~ 800 nm was due to surface defects. The peaks at $\lambda = 475$ nm and 500 nm in all three spectra were due to impurities present in hexane solvent as verified by collecting PL spectrum of hexane solvent.

Conversely, the optical properties of both the sandwiched nanorods were found to be different from those of the individual nanorods. As presented in *Figure 3.8a* for the ABA nanorods, there were two distinct absorption maxima at 524 nm and 645 nm that were consequential of CdS and CdSe band gap absorptions respectively. In *Figure 3.8c*, similarly, two absorption maxima at 490 nm and 614 nm were detected for the BAB nanorod. The slight blue shifts observed in the BAB nanorods are consistent with its shorter dimensions as confirmed from the TEM analysis (*Figure 3.2*).

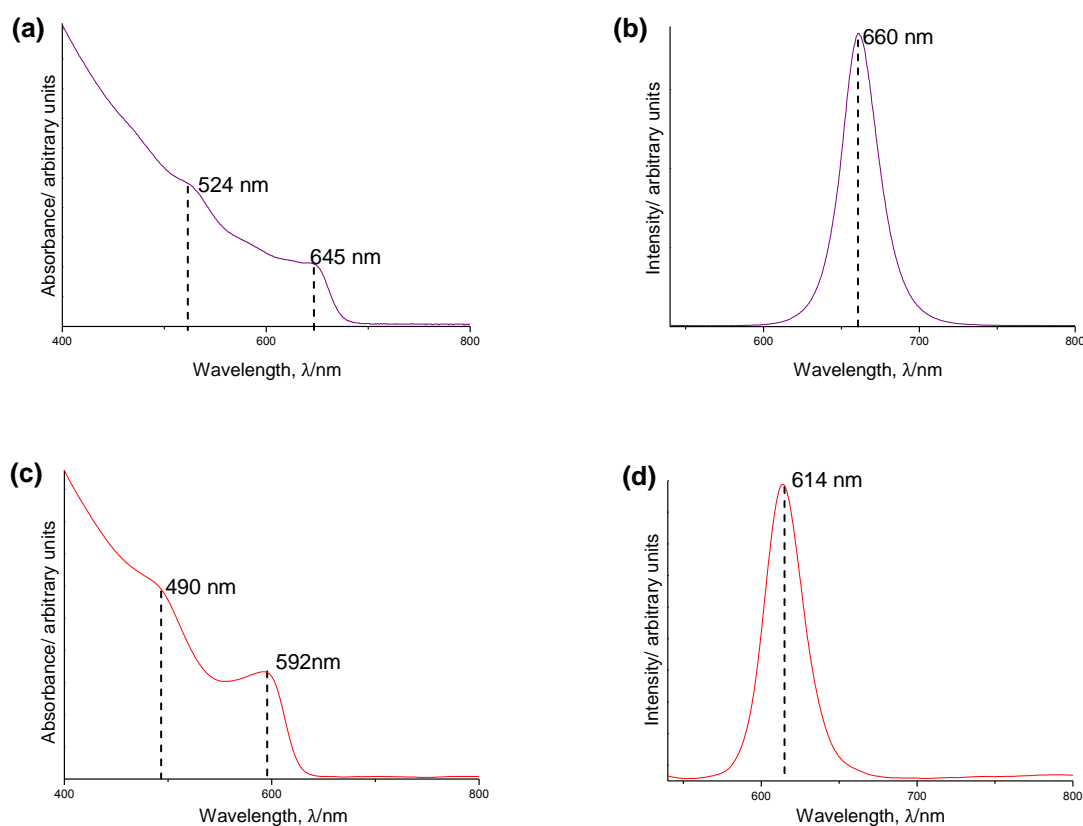


Figure 3.8. (a) & (c) UV-Vis and (b) & (d) PL ($\lambda_{excitation} = 525$ nm) spectra of the ABA (top, purple) and BAB (bottom, red) sandwiched nanorods respectively.

On the other hand, in *Figures 3.8b* and *3.8d* respectively, it was clear that there was only one peak attributable to CdSe emission in both the PL emission spectra. Contrasting this result with that of the physical mixture (*Figure 3.7c*), it is evident that there is electronic coupling between the segments in the sandwiched nanorods. Thus, while both the CdS and CdSe segments were excited in the sandwiched nanorods, the radiative relaxation of the excited electrons was that from the band gap of CdSe. The band alignments for the ABA nanorods resembled that of Type I core/shell structures (*Table 1.2*),¹² i.e. the exciton pairs generated are localized in CdSe due to its smaller band gap.¹³ The band alignments for the reverse nanorods resembled that of reverse-Type I core/shell structure.¹² Like their Type I counterparts, the exciton pairs also delocalize largely to the smaller band gap material,¹⁴ which in the context of our reverse BAB structure would be CdSe. We also noted that the full width half maximum of PL emission peaks of both types of nanorods were ~ 30 nm, and the diameters of the nanorods (6.8 ± 0.9 nm and 3.6 ± 0.6 nm respectively) were much smaller than the Bhor exciton diameter of bulk CdSe (9.1 nm¹⁵).

3.3 Deposition of Au on the CdS|CdSe|CdS and CdSe|CdS|CdSe sandwiched nanorods

Upon the successful synthesis of the sandwiched nanorods, we carried on with the investigation of the preferred deposition site(s) of Au nanoparticles on the two types of nanorods. There were three possible outcomes for the Au deposition as illustrated in *Figure 3.9*, using the ABA structure for exemplary purpose: (a) The Au nanoparticles would be randomly deposited along the entire length of the nanorods. (b)

The Au nanoparticles would be selectively deposited at the tips of the nanorods. (c) The Au nanoparticles would be selectively deposited at the segment of the nanorod with a smaller band gap (i.e. CdSe) which could act as an electron sink.¹

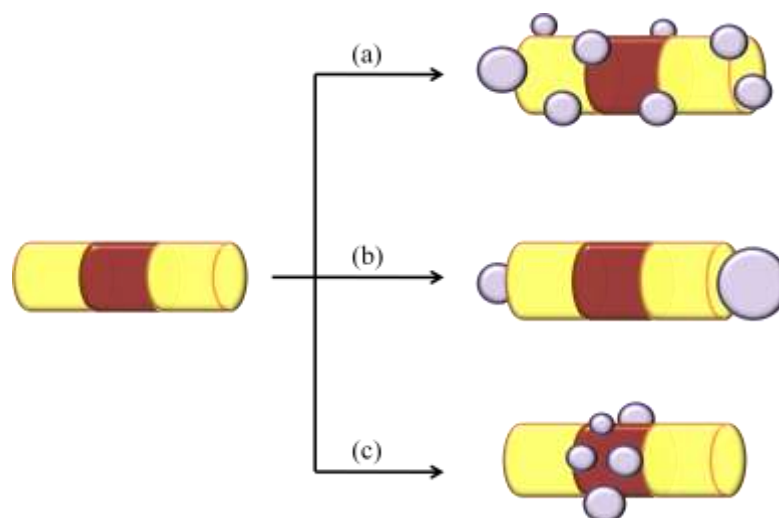


Figure 3.9. Possible morphologies for Au deposition on the ABA structure: (a) Au was deposited randomly along the nanorod, (b) Au was selectively deposited on the tips of the nanorod and (c) Au was selectively deposited on the lower band gap (CdSe) segment of the nanorod.

The deposition of Au nanoparticles was first performed on the as-synthesized ABA nanorods using a method adapted from Menagen *et al.*¹ We followed the deposition reaction over a period of 60 minutes, during which aliquots of the reaction mixture was extracted at 10 min, 30 min and 60 min intervals and quenched in hexane for analysis. The TEM images collected were shown in *Figure 3.10a-c*. It was noticed in general that, as the reaction duration lengthened, there was a change in the positions of the Au nanoparticles on the nanorods. Thus, whereas the Au

nanoparticles were initially randomly distributed along the sides of the nanorods, by the end of the 60th minute, lesser Au nanoparticles were detected along the sides while those at the tips of the nanorods appeared to have grown larger. We attempted to perform a statistical estimation of the size variation and tabulated the results as shown in *Table 3.1*. In *Figure 3.11*, three histograms reflecting the distribution of the Au nanoparticle normalized to the rod lengths were presented for the three aliquots extracted.

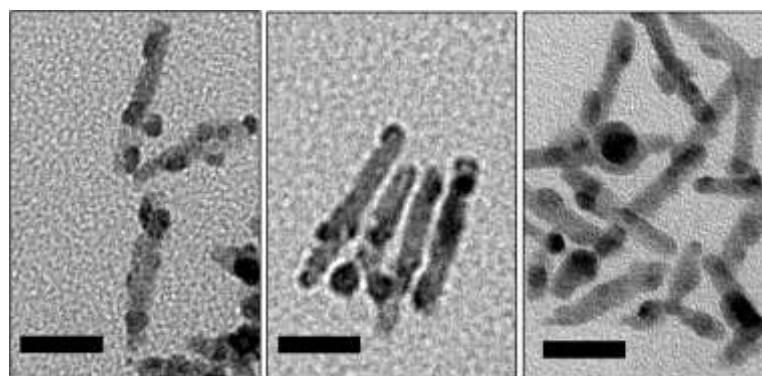


Figure 3.10. TEM images of Au deposition on the ABA nanorods at (a) 10 min, (b) 30 min and (c) 60 min after injection of Au precursor. All scale bars in the images are equivalent to 20 nm.

Table 3.1. Average diameter of Au nanoparticles on both the side facets and tips of the ABA nanorod at 10 min, 30 min and 60 min intervals after injection of Au precursor.

Time / min	Diameter Gold-Deposited Normal Structure / nm	
	Tip	Side
10	4.6 ± 1.7	3.1 ± 0.9
30	5.4 ± 1.7	3.1 ± 1.0
60	6.4 ± 1.4	2.5 ± 0.5

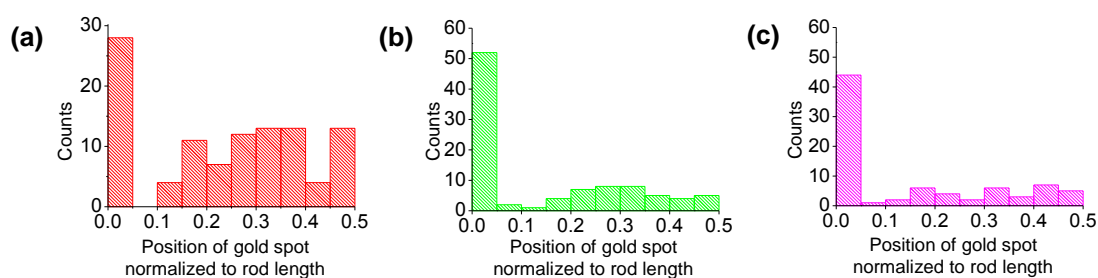


Figure 3.11. Distribution histograms relating the number of Au nanoparticles deposited on the various positions along the ABA nanorod at (a) 10 min, (b) 30 min and (c) 60 min after injection of Au precursor. The rod length was normalized to values between 0 and 0.5 inclusive. Value 0 indicates the nanorod tips from either end, value 0.5 indicates the middle of the nanorod length and all values between 0 and 0.5 indicate the nanorod side facets from either tip of the nanorod.

The Au deposition occurred initially at random positions of the nanorods. This suggested the strong influence of surface defects in directing the Au deposition along the sides of nanorods during the initial deposition stage. Even though CdSe had been suggested to play the role of electron sinks¹ due to its smaller band gap, the deposition of Au was evidently not selective to the CdSe segments of the ABA nanorods. There were two possible reasons behind this. Firstly, the deposition was carried out at ambient light and there might not have sufficient excited electrons to observe the electron sink effect. Secondly, the reduction of the Au precursors (Au^{3+} to Au) could have primarily occurred only due to the reducing dodecylamine (DDA) present, in a manner similar to that proposed by Capdevielle *et al.*¹⁶ for the reduction of Cu^{2+} to Cu^+ by primary amines. The Au precursors could be more easily reduced than the Cu

precursors since the standard reduction electrode potential involving cationic forms of Au is even more positive than that involving cationic forms of Cu.¹⁷

In a further study, we carried out a prolonged deposition of Au nanoparticles on the BAB nanorods. By the end of the 60th minute, we observed once again that the Au nanoparticles resided mainly at the tips of the nanorods (*Figure 3.12*), a result that was similar that on ABA nanorods. The observations of mainly tipped grown Au nanoparticles in both types of sandwiched nanorods suggested the occurrence of Ostwald ripening. Hence, due to the curvature morphology at the tip region of the nanorods, the tips have higher surface energy and would be the preferred site for ripening growth. This is regardless of whether the tips of the nanorods were sulfur-rich¹⁸ (the BAB structure) or not (the ABA structure). During Ostwald ripening, Au nanoparticles attached at the tips grew at the expense of the nanoparticles deposited originally at the defect sites along the nanorods.

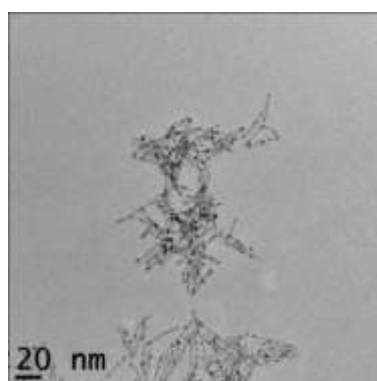


Figure 3.12. TEM image of Au deposition on the BAB nanorods 60 min after injection of Au precursor.

Finally, it is noteworthy that the deposition of Au was evidently not selective to the smaller band gap CdSe segments in both the ABA and BAB sandwiched nanorods. This observation thus did not support the postulation of electron sink effect. Nevertheless, in the following Section, we illustrate the existence of electronic coupling between the deposited Au and the sandwiched nanorods through their optical properties.

3.4 Optical properties of the Au-deposited CdS|CdSe|CdS and CdSe|CdS|CdSe sandwiched nanorods

In the literature, Au was known to either enhance or quench the emissions in different semiconductor nanoparticle systems.¹⁹⁻²¹ In *Figure 3.13*, it could be deduced that the Au deposition had quenched the original emissive properties of both the sandwiched nanorods. This effect could be explained as an efficient transfer of the photogenerated excited electrons from the sandwiched nanorods to the Au nanoparticles that led to a non-radiative relaxation.^{1,22}

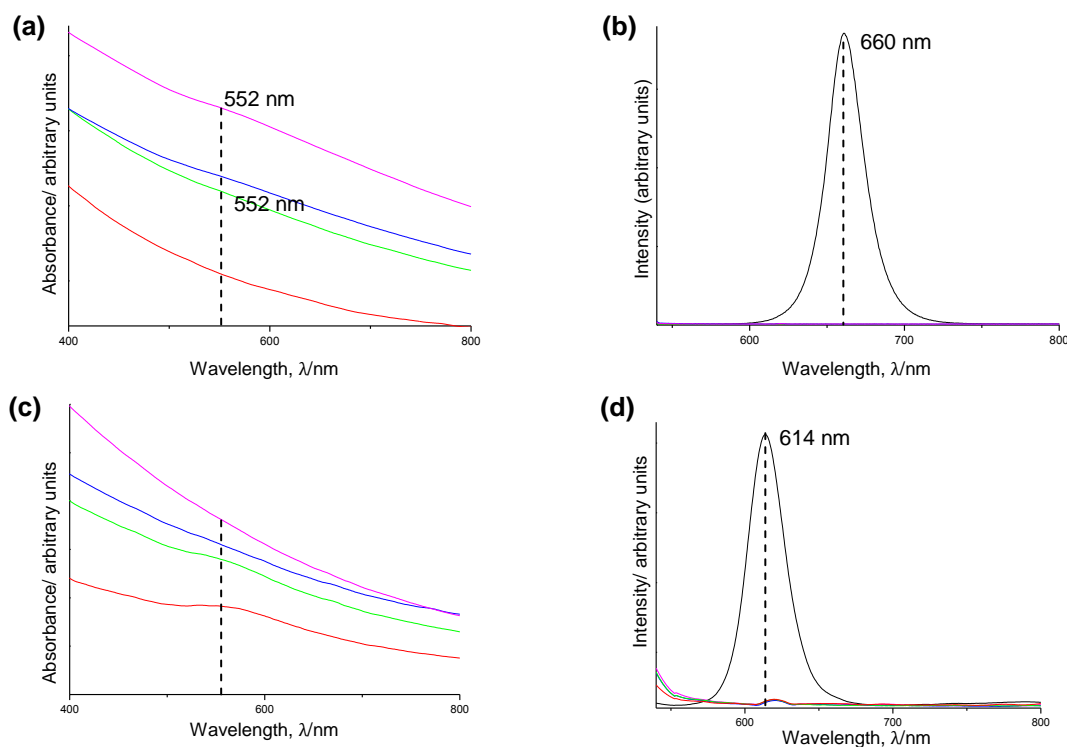


Figure 3.13. (a) & (c) UV-Vis and (b) & (d) PL ($\lambda_{excitation} = 525 \text{ nm}$) spectra of Au-deposited ABA (top) and BAB (bottom) nanorods at 10 min (red), 30 min (green), 45 min (blue) and 60 min (pink) after injection of the gold-precursor. The PL spectra of the original ABA and BAB nanorods were plotted in black in (b) & (d) respectively to illustrate the quenching of CdSe emission in the Au-deposited nanorods.

We further monitored the temporal evolution of the optical spectra during the deposition of Au as presented in *Figure 3.14*. For the Au-deposited ABA nanorods, CdS and CdSe absorptions were washed out at 13 and 28 minutes respectively after the addition of Au precursor. For the Au-deposited BAB nanorods, on the other hand, both the CdS and CdSe absorptions were washed out immediately upon the injection of Au precursor.

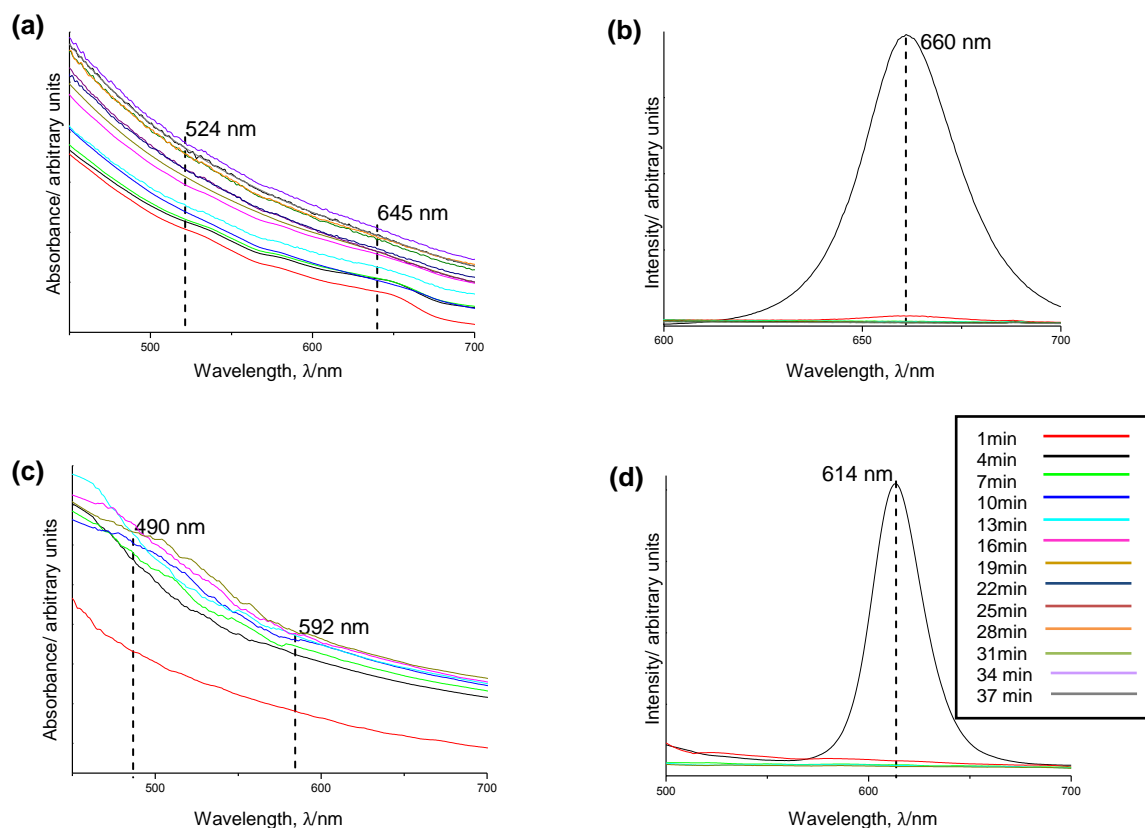


Figure 3.14. Temporal evolution of (a) & (c) UV-Vis and (b) & (d) PL ($\lambda_{excitation} = 420$ nm) spectra of Au deposition on the ABA (top) and BAB (bottom) nanorods monitored at three- and six-minute intervals respectively. The PL spectra of the nanorods were plotted in black in (b) & (d) respectively to illustrate the quenching of CdSe emission. The same time period legend applies to all four plots.

Thus, interestingly, the absorption feature to be washed out first corresponded to the segments that were at the two ends of the sandwiched structures. This suggested that interaction with Au nanoparticles was stronger with the tip segments of the nanorods, regardless of the chemistry of the end segment. More works could be undertaken to study the actual quenching mechanism of the PL emissions observed

for the Au-deposited nanorods because it could have been more complicated than what had been commonly perceived to be.

3.5 Summary

In summary, we had successfully synthesized the segmented nanorods, CdS|CdSe|CdS and CdSe|CdS|CdSe, and studied the deposition of Au on these heterostructures. The following are some observations derived from this study:

- (i) We observed that Au deposition first occurred randomly along the sides of nanorods suggesting defect growths. However, with an extended reaction period, Ostwald ripening possibly resulted in the final larger Au nanoparticles at the tip and fewer and smaller Au nanoparticles at the side.
- (ii) Electron sink effect due to the presence of smaller band gap CdSe segments was not evident.
- (iii) Our temporal monitoring of the optical properties of the Au-deposited nanorods revealed that the electronic structures of the nanorods might have been altered with the presence of Au.

3.6 References

- (1) Menagen, G.; Mocatta, D.; Salant, A.; Popov, I.; Dorfs, D.; Banin, U. *Chem. Mater.* **2008**, 3.
- (2) Menagen, G.; Macdonald, J. E.; Shemesh, Y.; Popov, I.; Banin, U. *J. Am. Chem. Soc.* **2009**, 6.
- (3) Chakraborty, S.; Yang, J. A.; Tan, Y. M.; Mishra, N.; Chan, Y. *Angew. Chem. Int. Ed.* **2010**, 5.
- (4) Saunders, A. E.; Popov, I.; Banin, U. *J. Phys. Chem. B* **2006**, 9.

- (5) Yeh, C.-Y.; Lu, Z. W.; Froyen, S.; Zunger, A. *Phys. Rev. B* **1992**, *46*, 12.
- (6) Murray, C. B.; Norris, D. J.; Bawendi, M. G. *J. Am. Chem. Soc.* **1993**, *115*, 10.
- (7) Lee, S.-M.; Cho, S.-N.; Cheon, J. *Adv. Mater.* **2003**, *15*, 4.
- (8) Peng, X.; Manna, L.; Yang, W.; Wickham, J.; Scher, E.; Kadavanich, A.; Alivisatos, A. P. *Nature* **2000**, *404*, 3.
- (9) Puzder, A.; Williamson, A. J.; Zaitseva, N.; Galli, G.; Manna, L.; Alivisatos, A. P. *Nano Lett.* **2004**, *4*, 5.
- (10) Wang, F.; Tang, R.; Buhro, W. E. *Nano Lett.* **2008**, *8*, 4.
- (11) Peng, Z. A.; Peng, X. *J. Am. Chem. Soc.* **2001**, *123*, 2.
- (12) Reiss, P.; Protiere, M.; Li, L. *Small* **2009**, *5*, 15.
- (13) Steiner, D.; Dorfs, D.; Banin, U.; Sala, F. D.; Manna, L.; Millo, O. *Nano Lett.* **2008**, *8*, 5.
- (14) Battaglia, D.; Li, J. J.; Wang, Y.; Peng, X. *Angew. Chem. Int. Ed.* **2003**, *42*, 5.
- (15) Pokutnii, S. I. *Semiconductors* **2010**, *44*, 6.
- (16) Capdevielle, P.; Lavigne, A.; Sparfel, D.; Baranne-Lafont, J.; Cuong, N. K.; Muaumy, M. *Tetrahedron Lett.* **1990**, *31*, 4.
- (17) Bard, A. J.; Parsons, R.; Jordan, J. *Standard Potentials in Aqueous Solutions*; Marcel Dekker: New York, 1985.
- (18) McBride, J.; Treadway, J.; Feldman, L. C.; Pennycook, S. J.; Rosenthal, S. J. *Nano Lett.* **2006**, *6*, 6.
- (19) Lee, A.; Coombs, N. A.; Gourevich, I.; Kumacheva, E.; Scholes, G. D. *J. Am. Chem. Soc.* **2009**, *131*, 7.
- (20) Kulakovich, O.; Strekal, N.; Yaroshevich, A.; Maskevich, S.; Gaponenko, S.; Nabiev, I.; Woggon, U.; Artemyev, M. *Nano Lett.* **2002**, *2*, 4.
- (21) Hosoki, K.; Tayagaki, T.; Yamamoto, S.; Matsuda, K.; Kanemitsu, Y. *Phys. Rev. Lett.* **2008**, *8*, 4.
- (22) Mokari, T.; Rothenberg, E.; Popov, I.; Costi, R.; Banin, U. *Science* **2004**, *304*, 4.

Chapter 4

Gold Deposition on CdS/ZnS:Mn²⁺ Doped-and-Seeded Heterostructured Nanocrystals

As mentioned in Chapter 1, an adequate understanding of the synthesis and interaction between multi-component hybrid nanocrystals (HNCs) is essential in our employment of the diverse potentials of HNCs. The rational designing and synthesis of an assortment of HNCs with different properties are made possible through the understanding of the reactivity of the crystal faces present in different crystal structures of the nanocrystals. In particular, Au nanocrystals have been demonstrated to have the ability in quenching or enhancing the photoluminescence of semiconductor nanocrystals, depending on whether plasmon-exciton coupling or energy transfer between Au and the nanocrystals is at work.¹⁻⁴ Mn²⁺ dopants, on the other hand, usually result in quenching of band gap emissions as seen in the numerous experimental examples through an energy transfer process from the host nanocrystal to the dopants.^{5,6}

In the previous chapter, our investigation on two-component sandwiched semiconductor nanorods decorated with gold nanocrystals was presented. In this chapter, the gold deposition study was extended further to a doped-and-seeded CdS/ZnS:Mn²⁺ nanorod system. There had been relatively few reports on the interactions and optical properties of multi-component nanocrystals comprising of both doped and seeded components. We report here synthesis methodologies that offer reasonable step-wise modification and monitoring, from single-component CdS

nanocrystals (*Section 4.1*), heterostructured CdS/ZnS seeded nanorod (*Section 4.2*), doped-and-seeded CdS/ZnS:Mn²⁺ nanorod (*Section 4.3*), and finally to the hybrid Au-CdS/ZnS:Mn²⁺ nanocrystals system (*Section 4.4*).

4.1 Synthesis and characterization of the CdS seeds

The CdS seeds were synthesized via the decomposition of CdTB, in the presence of HDA at CdTB-to-HDA molar ratio of 1:40 (details given in *Section 2.2.5*). In studies that were previously conducted by our research group,⁷ it was found that HDA played a dual role as nucleophile and capping agent due to the presence of a lone pair of electrons on the N atom. This synthesis method was advantageous because it circumvented the need of a long reaction time (up to ten hours)⁸ and/or high reaction temperature (typically more than 250 °C)⁹ used in most other previously reported methods.

TGA was conducted under a nitrogen atmosphere to have a better understanding of the effects of temperature on CdTB. As seen from *Figure 4.1*, the most significant weight loss was observed between 175 °C and 340 °C. The weight started to stabilize above 340 °C, with residual weight of 38.0 %, which corresponded to the molar mass of CdS. From this result, it could be inferred that temperature required to decompose CdTB should be higher than 175 °C. However, in the presence of amine, such as HDA, which functioned as the nucleophilic activating agent, lower decomposition temperature can be used. As the CdTB was dissolved in TOP, which was a coordinating solvent and had a stabilization effect on the precursor, optimized temperature for the experiment was 120 °C.

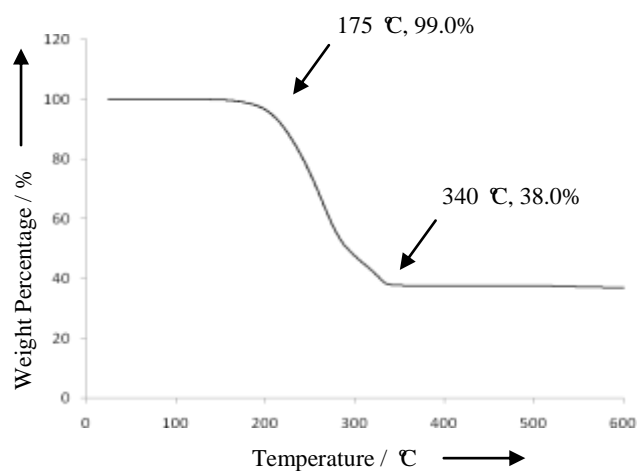


Figure 4.1 TGA curve for the decomposition of CdTB precursor from room temperature to 600 °C.

Optical properties of the CdS nanocrystals synthesized were as reflected in *Figure 4.2a*. The absorption plot in red revealed that the CdS band gap absorption was at ~ 440 nm and its corresponding PL emission peak shown in black was at ~ 477 nm. The broad PL emission observed beyond 600 nm was a result of surface defects present on the quantum dots. The presence of defects was not unexpected as the surfaces of the CdS nanocrystals were only poorly passivated by HDA. The capping agent had poor packing efficiency and would also bind preferentially to only the cationic surfaces instead of the entire surface.

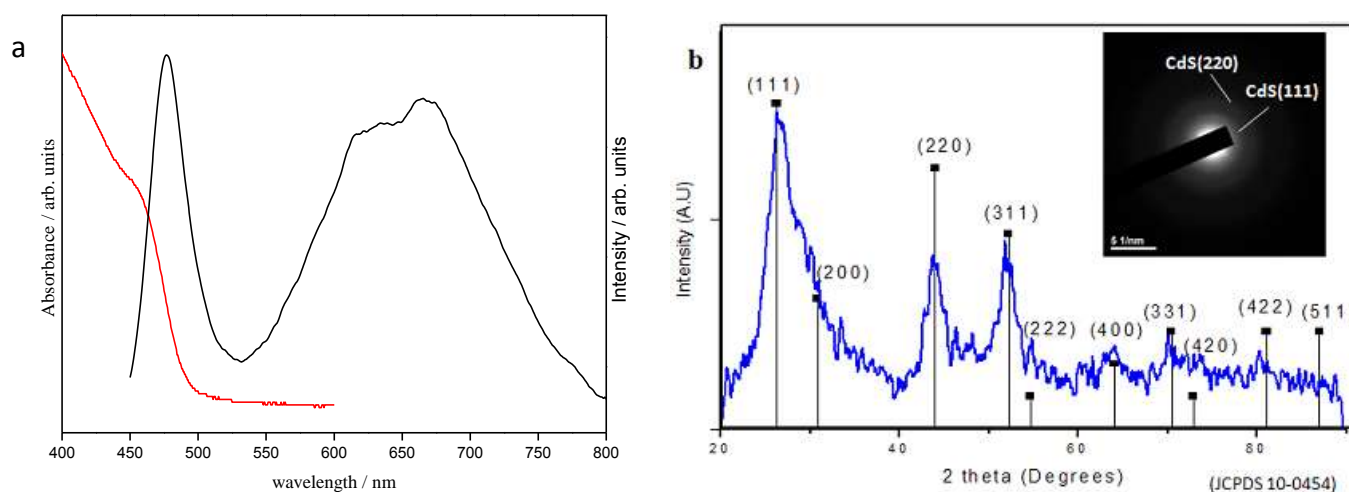


Figure 4.2. (a) UV-Vis absorption (red line) and PL (black line) spectrum ($\lambda_{ex} = 280$ nm) of the CdS seeds prepared. The band gap absorption was at 440 nm and the corresponding emission showed a Stoke's shift of ~ 37 nm. The presence of surface defects on the seeds resulted in the broad emission in the range of ~ 550 nm to ~ 750 nm. (b) XRD pattern of the CdS seeds fitted to the zinc blende standard JCPDS 10-0454. Inset: SAED pattern of the CdS seeds.

As seen from the XRD pattern (Figure 4.2b), the characteristic wurtzite triplet peak was clearly absent within the 2θ range between 25° to 30° . In addition, the sharp peaks observed at 2θ values of $\sim 26^\circ$, 44° and 52° could be indexed to the (111), (220) and (311) planes respectively of the zinc blende CdS. The SAED pattern (inset of Figure 4.2b) collected also presented a similar finding on the CdS phase, supporting that the quantum dots obtained were indeed of zinc blende phase, which was also the most stable crystallographic phase of CdS obtained at low synthesis temperature (lower than 250°C).^{10,11} The centrosymmetric zinc blende phase was

instrumental in promoting isotropic growth of the nuclei to yield nearly spherical quantum dots.

4.2 Synthesis and characterization of the CdS/ZnS seeded nanorods

Following the synthesis of CdS, a seeded growth approach with ZnTB as the precursor for ZnS, was adopted to yield CdS-seeded ZnS nanorods (denoted as CdS/ZnS hereafter). During the reaction, it is important to suppress the formation of ZnS nuclei to prevent the formation of individual ZnS nanorods. Thus, the synthesis was carried out over temperature range of 60 °C to 250 °C, during which the gradual heating process provided a condition mild enough to prevent homogenous nucleation of ZnS particles.¹² Heterogeneous nucleation was induced, with the as-synthesized CdS quantum dots functioning as the nucleation sites for the ZnS monomers. This led to the enveloping of CdS with ZnS during the initial nucleation step. On the other hand, the reaction conditions was optimized such that it provided continual and sufficiently high monomer concentration, thus enabling 1-D diffusion growth¹³ of the shell layer and favored nanorods formation. It is worth highlighting that this synthesis methodology only required one capping agent to achieve rod-shaped and seeded nanocrystals. This offers great simplicity in synthesis as compared to the more commonly seen examples^{12,14,15} relying on a mixture of capping agents to attain preferential growth into nanorods.

HRTEM was employed to characterize the structure of the synthesized seeded nanorods. From the HRTEM image (*Figure 4.3a*) obtained, lattice fringes identified can be assigned to the CdS (200) and ZnS (111) planes. In addition, the CdS seeds

were observed to be positioned off-centre along the long axis of the ZnS nanorod. This kind of asymmetrical growth is commonly observed among seeded rods due to unequal growth rate at the two ends of the nanorods.¹⁶

One absorption peak was exhibited in the UV/Vis absorption spectrum (*Figure 4.3b*, red line) at ~ 305 nm, this could be assigned to the band gap absorption of the ZnS nanorod. The presence of only ZnS absorption could be understood by taking into account the relatively higher molar absorptivity of ZnS¹⁷ compared to CdS.¹⁸ On top of that, the amount of ZnS greatly exceeded the amount of CdS present since the feed ZnTB-precursor-to-CdS ratio was 100:1.

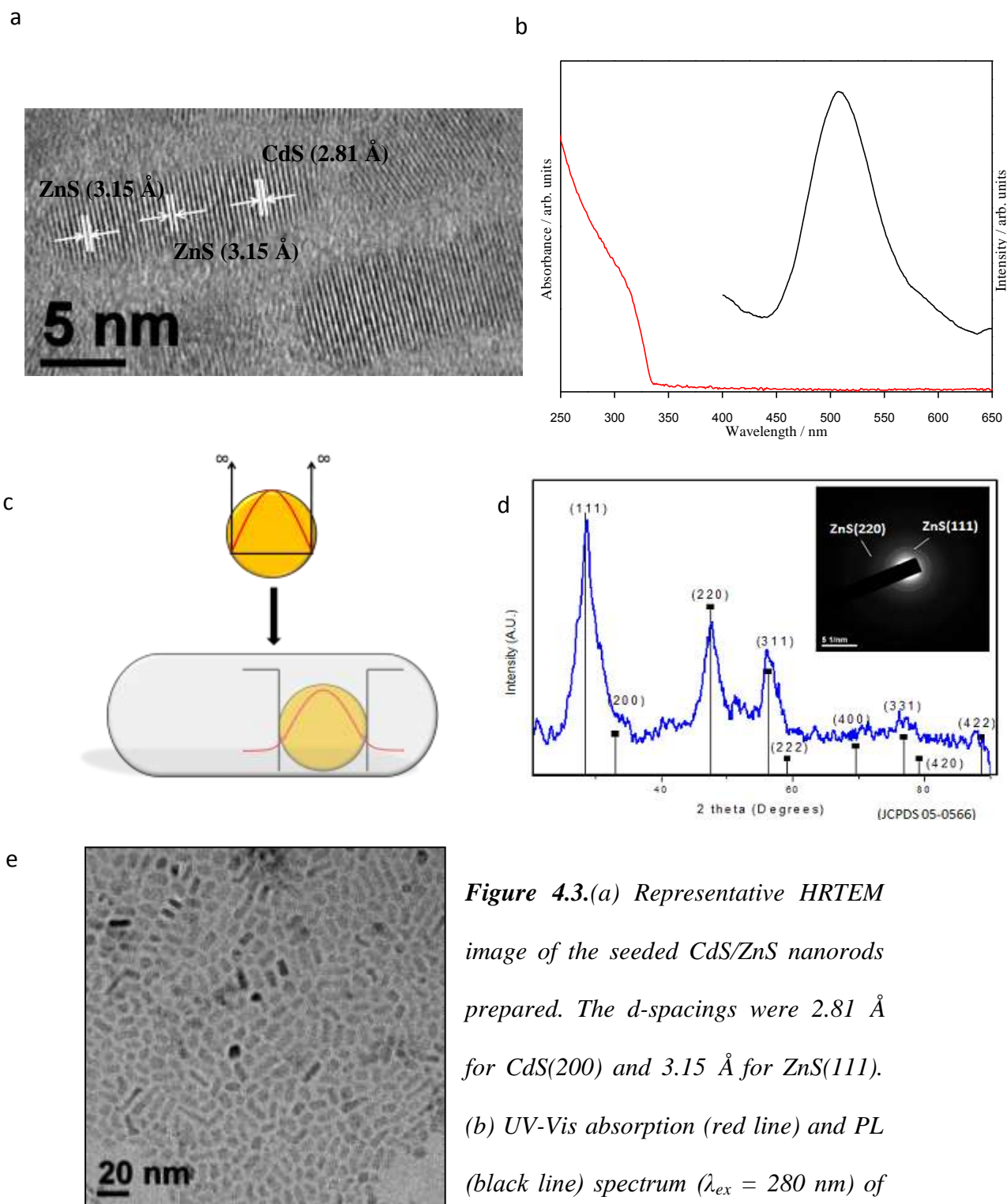


Figure 4.3. (a) Representative HRTEM image of the seeded CdS/ZnS nanorods prepared. The d -spacings were 2.81 Å for CdS(200) and 3.15 Å for ZnS(111). (b) UV-Vis absorption (red line) and PL (black line) spectrum ($\lambda_{ex} = 280$ nm) of the CdS-seeded ZnS nanorods. The ZnS band gap absorption was at ~ 305 nm while the CdS band gap emission was centred at ~ 500 nm. (c) Cartoon illustrating the change in wave function as the ZnS nanorod was overgrown on the

CdS seeds. The wave function 'leaked' into the ZnS nanorod region after it encompassed the CdS. (d) XRD patterns of the CdS/ZnS nanorods prepared fitted to JCPDS: 05-0566. Inset showed the SAED pattern. (e) Representative TEM image of the CdS/ZnS prepared.

Whereas the UV/Vis absorption property of the seeded nanorod was mainly due to the ZnS rod, the PL emission was due to the CdS seed, as observed in the PL spectrum (*Figure 4.3b*, black line) which comprised of a peak that centred at ~ 500 nm. This interesting optical phenomenon could be explained by the maximum overlap between the exciton pair wave functions at the location of the seed which then strongly favoured radiative exciton recombination to take place at CdS.¹⁹ The PL spectrum had another feature: the PL emission of CdS seeds in CdS/ZnS had a red-shifted (~ 23 nm) from ~ 477 (in uncoated CdS) nm to ~ 500 nm. This observation can be accounted for using the particle-in-a-box model. In a bare CdS quantum dot, exciton pairs were predictably trapped in a “zero-dimensional box” bounded by infinite energy walls. As such, the electron wave function is trapped entirely within CdS. However, in the case of CdS/ZnS, the boundaries of the exciton pairs would be replaced by finite energy walls due to the presence of ZnS overcoat. When that happened, the electron wave functions would be able to “leak” into the ZnS shell, lowering the peak maxima of the wave function, thus resulting in the red-shifted PL emission.

The result from the XRD analysis of the seeded nanorods was shown in *Figure 4.3d*. The three distinctly singlet peaks as reflected in the spectrum could be matched to the (111), (220) and (311) planes of zinc blende ZnS. Furthermore, the

SAED pattern obtained (inset of *Figure 4.3d*) also revealed the same phase information. Together with the phase information of CdS seeds aforementioned, it was interpreted that there was a coherent epitaxial growth of ZnS on CdS.

4.3 Synthesis and characterization of the CdS/ZnS:Mn²⁺ doped-and-seeded nanorods

In this Section, we doped the ZnS nanorods covering CdS seeds above with Mn²⁺ ions. As far as we know, this is the first example of seeded-and-doped nanorod system reported. We are interested to investigate if the presence of dopants in the nanorods will affect the optical properties of the seeded nanorods.

From the TEM image (*Figure 4.4a*) collected, we observed that the incorporation of Mn²⁺ ions into ZnS did not result in any significant change in the size and morphology of the nanorods (compared to the undoped nanorods in *Figure 4.3*). This was quite expected due to the relatively small amount of Mn²⁺ ions doped, which will not cause any significant lattice strain on the nanorods on the whole. This observation has confirmed that our one-pot synthesis method (*Section 2.2.6*) was capable in retaining the rod-shaped morphology of ZnS while introducing the dopants.

Comparatively, the CdS/ZnS:Mn²⁺ nanorods shared a similar ~ 305 nm UV/Vis absorption peak (*Figure 4.4b, red line*) with their CdS/ZnS counterparts (*Figure 4.3b*). However, these doped nanorods exhibited starkly different PL emission spectrum (*Figure 4.4b, black line*) from the undoped ones. Thus, a new PL peak at ~ 585 nm appeared while the PL peak at ~500 nm corresponding to CdS band gap emission has disappeared.

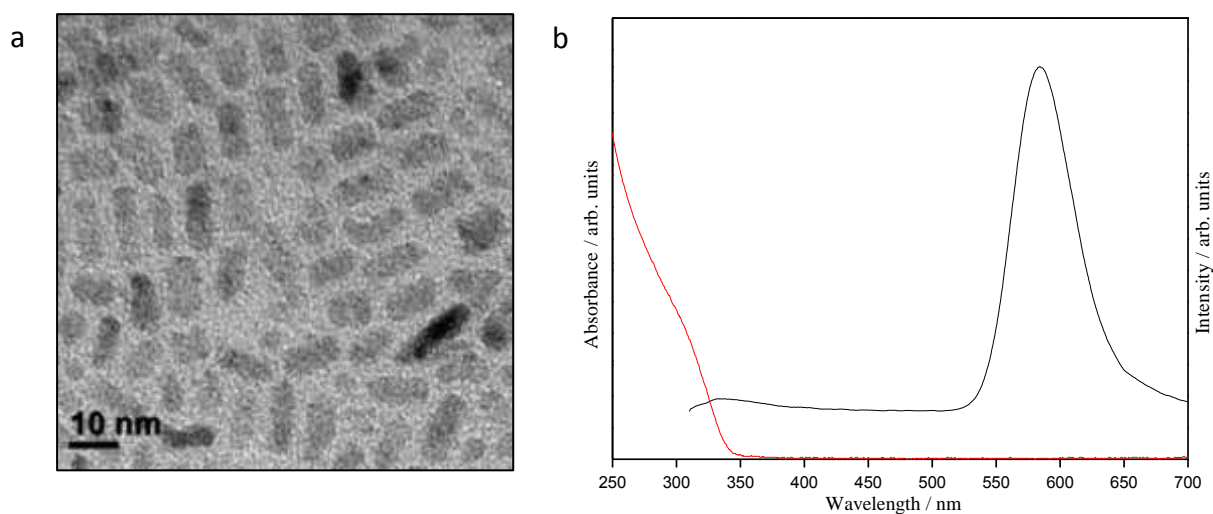


Figure 4.4. (a) Representative TEM image of the CdS-seeded Mn^{2+} -doped ZnS nanorods, CdS/ZnS:Mn^{2+} . (b) UV-Vis absorption (red line) and PL emission (black line) spectrum ($\lambda_{\text{ex}} = 280 \text{ nm}$) of the CdS/ZnS:Mn^{2+} nanorods, CdS/ZnS:Mn^{2+} , showing characteristic ${}^4T_1 \rightarrow {}^6A_1$ emission of Mn^{2+} at $\sim 585 \text{ nm}$.

The $\sim 585 \text{ nm}$ PL emission peak could be assigned to the distinctive relaxation from the metastable excited state to the ground state (${}^4T_1 \rightarrow {}^6A_1$) of Mn^{2+} ions. The appearance of this PL emission peak was indicative of a successful doping of the seeded nanorods. If the Mn^{2+} ions existed as free ions instead, they would not be emissive because of the large amount of energy required for a spin-forbidden excitation for the free ions.²⁰ It should be noted that the absence of the Mn^{2+} absorption in the UV/Vis absorption spectrum recorded did not conflict with our deduction of a successful doping because the absorption cross-section of Mn^{2+} is typically at least 10^4 times less than that for the semiconductor nanocrystals.²⁰ In fact, there were three reasons for us to expect the easy doping of Mn^{2+} ions into the ZnS

layer. Firstly, theoretical works by Erwin et al.²¹ had already shown that the planes present in zinc blende ZnS had binding energies with Mn^{2+} adsorbates that were even higher than that present in bulk crystalline Mn. Secondly, the nanorods' relatively large size, compared with typical semiconductor quantum dots, led to a lower formation energy for the dopant.²² Thirdly, amine-based capping ligands generally had lower binding energy with Mn^{2+} dopants,²³ which in turn translated to easier dopant adsorption on the nanorod surfaces and subsequently a greater likelihood for the incorporation into the nanorods. All these three factors explained the successful in the formation of seeded and doped *zb*-CdS/*zb*-ZnS: Mn^{2+} nanorods.

The disappearance of the CdS band gap emission could be rationalized together with the appearance of the characteristic Mn^{2+} emission peak. This phenomenon suggested an efficient energy transfer process from the seeded nanorods to the Mn^{2+} dopants (*Figure 4.5*). The energy transfer was made possible by the spin-orbit coupling between the Mn^{2+} and S^{2-} .²⁴ It was proposed that the energy transfer process started with a rate-determining Forster-type transfer from the exciton pairs in CdS to bound excitons localized around the dopants. Subsequently, an energy transfer, mediated through dipole-dipole interactions, from the bound excitons to the dopants happened which eventually resulted in the radiative relaxation that the dopants underwent.⁶

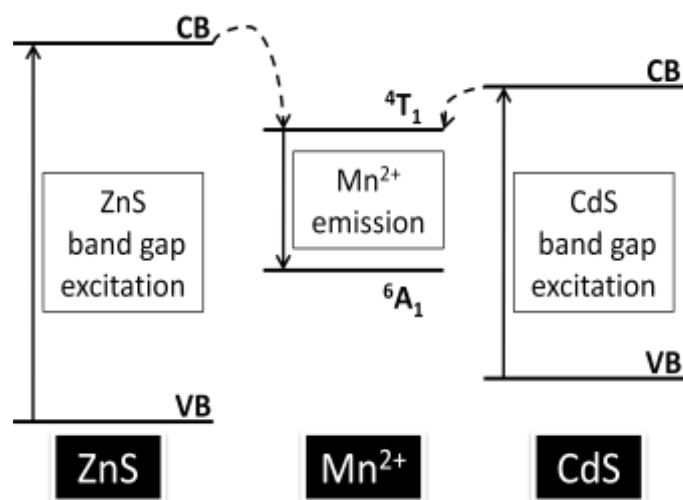


Figure 4.5. Schematics showing energy transfer from ZnS host and CdS to Mn^{2+} dopants. CB represents conduction band and VB represents valence bands.

The asymmetrical peak profile of the ${}^4T_1 \rightarrow {}^6A_1$ transition in *Figure 4.4b* also provided additional information of the CdS/ZnS: Mn^{2+} system. It was reported²⁵ that the Mn-S bond lengths were shorter at the sub-surface region, which resulted in a lifting of degeneracy of the energy states in Mn^{2+} ions that led to a smaller energy gap between the 4T_1 and 6A_1 states. The observation of a tailing emission peak thus suggested that most of the Mn^{2+} ion resided near the surface and emitted at a slightly longer wavelength.

4.4 Gold deposition on the CdS/ZnS: Mn^{2+} Hybrid Nanorods

In this Section, we desired to study changes in the optical properties of the nanorods in the presence of both Au and Mn^{2+} , as both were expected to alter the optical properties of nanocrystals but in different ways. The excitation mechanism of Mn^{2+} dopants involved a rate-determining Forster energy transfer from excitons

generated in nanocrystals to bound excitons in the dopants via dipole-dipole interaction.⁶ As such, the proportion of band gap relaxation for the excitons would be greatly decreased and the semiconductor band gap emission would be quenched. On the other hand, a transfer of electrons from the conduction band of excited nanocrystals to the Au nanocrystals was expected to quench the band gap PL emissions of the semiconductor nanocrystals.²⁶

We surmised that when both Au and Mn^{2+} were to be present in the same nanorods, electrons would be transferred to the Au after the nanorods were excited. As such, there would be a lack of available excitons for the excitation of Mn^{2+} dopants, leading to an efficient quenching of the Mn^{2+} dopant emissions. To test this hypothesis, we prepared Au-CdS/ZnS: Mn^{2+} and compared the PL emission properties of the nanorods before and after the Au-deposition, i.e. CdS/ZnS: Mn^{2+} and Au-CdS/ZnS: Mn^{2+} .

The gold deposition was performed in the same way as presented in *Section 2.2.3*. Typical TEM image was shown in *Figure 4.6a*. For a fair comparison, the samples studied were adjusted to the same concentration through their UV/Vis absorbance values (difference < 0.03). As seen in *Figure 4.6b*, the Mn^{2+} dopant emission was totally quenched after Au nanocrystals were attached onto the seeded-and-doped nanorods. This observation was similar to that reported by Ma and Chen on silica-coated Au nanoparticles with ZnS: Mn^{2+} nanoparticles attached onto the silica.²⁷ In our case, however, the Au nanocrystals were directly attached to the doped nanocrystals, and not separated by a layer of silica.²⁷ This thus could offer more insights to the actual interaction between the doped nanocrystals with Au nanocrystals when they were directly in contact. These results confirmed our hypothesis that the

excited electrons generated from the band gap absorption would be preferentially transferred to the Au nanocrystal instead of an energy transfer to the transition metal dopant ions. We postulate that this could be due to a quicker kinetics for the transfer of electrons to the Au nanocrystals compared to energy transfer to the dopant.

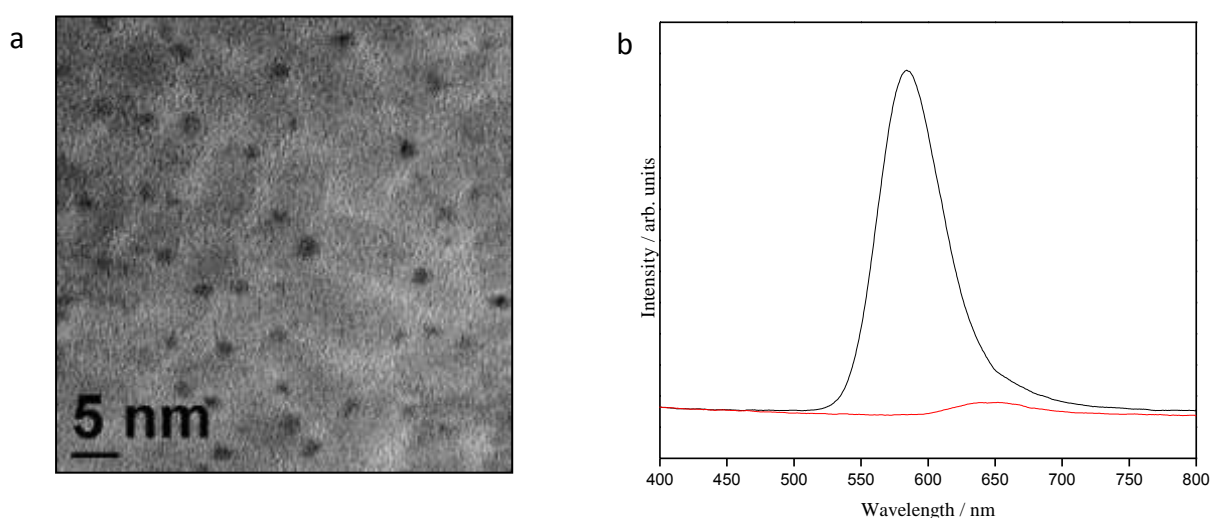


Figure 4.6. (a) Representative TEM image of Au decorated nanorods, Au-CdS/ZnS:Mn²⁺. The spherical regions with a darker contrast revealed regions of Au nanocrystals. (b) PL spectrum of CdS/ZnS:Mn²⁺ (black) and Au-CdS/ZnS:Mn²⁺ (red) ($\lambda_{ex} = 280$ nm), showing the quenching of Mn²⁺ emission upon Au deposition.

4.5 Summary

A series of synthesis steps were presented that had the strengths of being simple and less demanding in terms of time and temperature required. Through this series of syntheses, we had successfully and step-wisely increased the number of components present in the HNC system to investigate the effects of each component on the optical properties displayed by the system. We have confirmed that the PL emission properties of the HNCs could be altered systematically by adding

components to the nanocrystals. The observation and understanding of the system is largely aided by the ability to add the component one after the other during rational stepwise synthesis.

In particular, we presented an important case study which involved the simultaneous presence of two potential quenchers (Au and Mn^{2+} dopants) of semiconductor band gap emissions on the same HNC system. We observed that the Au nanocrystals were better quenchers than the Mn^{2+} dopants, possibly due to the efficient migration of electrons from the semiconductor to the Au particles.

4.6 References

- (1) Lakowicz, J. R. *Anal. Biochem.* **2001**, 298, 1.
- (2) O. Kulakovich, N. S., A. Yaroshevich, S. Maskevich, S. Gaponenko, I. Nabiev, U. Woggon, M. Artemyev *Nano. Lett.* **2002**, 2, 1149.
- (3) A. Lee, N. A. C., I. Gourevich, E. Kumacheva, G. D. Scholes *J. Am. Chem. Soc.* **2009**, 131, 10182.
- (4) K. Hosoki, T. T., S. Yamamoto, K. Matsuda, Y. Kanemitsu *Phys. Rev. Lett.* **2008**, 100, 207404(1).
- (5) Tanaka, M.; Qi, J.; Masumoto, Y. *Solid State Commun.* **2001**, 120, 7.
- (6) Y. Yang, O. C., A. Angerhofer, Y. C. Cao *Chem. Eur. J.* **2009**, 15, 3186.
- (7) Lim, W. P.; Zhang, Z.; Low, H. Y.; Chin, W. S. *Angew. Chem. Int. Ed.* **2004**, 43, 5.
- (8) Y. Chen, Z. R. *Anal. Chem.* **2002**, 74, 5132.
- (9) Z. A. Peng, Z. P. *J. Am. Chem. Soc.* **2001**, 123, 183.
- (10) Zelaya-Angel, O.; Alvarado-Gil, J. J.; Lozada-Morales, R. *Appl. Phys. Lett.* **1994**, 64, 291.
- (11) S.-M. Lee, S.-N. C., J. Cheon *Adv. Mater.* **2003**, 15, 441.

-
- (12) P. D. Cozzoli, T. P., L. Manna *Chem. Soc. Rev.* **2006**, 35, 1195.
- (13) Z. A. Peng, X. P. *J. Am. Chem. Soc.* **2001**, 123, 1389.
- (14) Peng, X.; Manna, L.; Yang, W.; Wickham, J.; Scher, E.; Kadavanich, A.; Alivisatos, A. P. *Nature* **2000**, 404, 59.
- (15) A. E. Saunders, I. P., U. Banin *J. Phys. Chem. B* **2006**, 110, 25421.
- (16) L. Carbone, C. N., M. De Giorgi, F. D. Sala, G. Morello, P. Pompa, M. Hytch, E. Snoeck, A. Fiore, I. R. Franchini, M. Nadasan, A. F. Silvestre, L. Chiodo, S. Kudra, R. Cingolani, R. Krahne, L. Manna *Nano. Lett.* **2007**, 7, 2942.
- (17) A. Jaiswal, P. S., A. Chattopadhyay, S. S. Ghosh *Plasmonics* **2010**, *Article-in-press*, 1.
- (18) W. William Yu, L. Q., W. Guo, X. Peng *Chem. Mater.* **2003**, 15, 2854.
- (19) E. Yoskovitz, G. M., A. Sitt., E. Lachman, U. Banin *Nano. Lett.* **2010**, 10, 3068.
- (20) Beaulac, R.; Archer, P. I.; Ochsenein, S. T.; Gamelin, D. R. *Adv. Funct. Mater.* **2008**, 18.
- (21) S. C. Erwin, L. Z., M. I. Haftel, A. L. Efros, T. A. Kennedy, D. J. Norris *Nature* **2005**, 436, 91.
- (22) G. M. Dalpian, J. R. C. *Phy. Rev. Lett.* **2006**, 96, 226802(1).
- (23) M.-H. Du, S. C. E., Al. L. Efros *Nano. Lett.* **2008**, 8, 2878.
- (24) Boulanger, D.; Parrot, R.; Cherfi, Z. *Phy. Rev. B* **2004**, 70.
- (25) A. Nag, R. C., P. Mahadevan, A. V. Gopal, A. Hazarika, A. Mohan, A. S. Vengurlekar, D. D. Sarma *J. Phys. Chem. C* **2010**, 114, 18323.
- (26) R. Costi, A. E. S., E. Elmalem, A. Salant, U. Banin *Nano. Lett.* **2008**, 8, 637.
- (27) L. Ma, W. C. *J. Appl. Phys.* **2010**, 107, 123513(1).

Chapter 5

Conclusions and Outlook

In light of the achievements in understanding and controlling the synthesis of single-material nanocrystals, research trend has clearly shifted towards studying multi-component nanocrystals that promised varied functionalities and scientific interests. Broadly speaking, the works covered in this thesis are in cognisance of the trend and are designed to help better understand the control and modification of the structural and optical properties of multi-component nanocrystals.

Instead of working on the commonly used seeded nanorod HNCs, we have chosen to study the deposition of gold on nanorods with CdS-CdSe sandwiched structures in Chapter 3. We believed that sandwiched nanorods can act as better test samples for the different hypotheses proposed. We have found that the positions of Au nanoparticles deposition were affected by the duration of which the experiment was carried out. Au nanoparticles were found to deposit along the sides of the nanorods initially. Ostwald ripening occurred with longer duration of the experiment to yield bigger gold nanoparticles at tips of the nanorods.

Interesting optical properties were observed too. Monitoring of the temporal evolution of the optical properties revealed that the Au nanoparticles interacted more strongly with materials that formed the end segments of the sandwiched nanorods, regardless of whether it was CdS or CdSe.

Chapter 4 documented a series of work that involved a novel, systematic and stepwise modification of structural and optical properties of nanocrystals. Starting from single-material CdS nanocrystals, we gradually increased the complexity of the structure by coating the CdS with ZnS in the form of a rod, followed by doping the shell with Mn^{2+} ion and lastly by depositing Au nanoparticles. The variations in optical properties with each structural change were also recorded. A red-shift in the CdS band gap emission when CdS was the seeds were enveloped by ZnS rod was observed. On the other hand, after doping the nanocrystals with Mn^{2+} , the Mn^{2+} -related emission was the most prominent feature in PL spectrum. Lastly, the presence of Au nanocrystals resulted in effective quenching of all PL emissions. The results collected laid the grounds for further investigations of the mechanisms that are causing the various changes in the optical properties.

Thus far, the proverbial abilities of dopants and gold nanoparticles in quenching the PL emission of the host semiconductor nanocrystals are mostly studied independently; few studies have worked on directly comparing the two quenchers in a single system and it is therefore a research area that can be explored. From a broader perspective, the take-away point is that there could be more works conducted to directly compare different classes of materials that exhibit similar properties. The overall property may be synergistic or otherwise. In fact, new properties may even emerge.

In the case of multi-component nanocrystals, theoretical explanations offered for observations tend to be unique to individual systems under discussion. In other

words, there is an apparent lack of a unified theory that can explain the science underpinning the observed properties of multi-component nanocrystals well. Further research could aim at translating our *a posteriori* knowledge into a more powerful *a priori* understanding. This would lend better guidance in our design protocols for the syntheses of different multi-component nanocrystals that are essential to fully maximize the potentials and applications of such HNCs.